

# Nature of Adsorption on TiC(111)

Carlo Ruberto\* and Bengt I. Lundqvist

*Department of Applied Physics, Chalmers University of Technology, SE-412 96 Göteborg, Sweden*

Extensive density-functional calculations are performed for chemisorption of atoms in the three first periods (H, B, C, N, O, F, Al, Si, P, S, and Cl) on the polar TiC(111) surface. Calculations are also performed for O on TiC(001), for full O( $1 \times 1$ ) monolayer on TiC(111), as well as for bulk TiC and for the clean TiC(111) and (001) surfaces. Detailed results concerning atomic structures, energetics, and electronic structures are presented. For the bulk and the clean surfaces, previous results are confirmed. In addition, new detailed results are given on the presence of C–C bonds in the bulk and at the surface, as well as on the presence of a Ti-based surface resonance (TiSR) at the Fermi level and of C-based surface resonances (CSR's) in the lower part of the surface upper valence band (UVB). For the adsorption, adsorption energies  $E_{\text{ads}}$  and relaxed geometries are presented, showing great variations characterized by pyramid-shaped  $E_{\text{ads}}$  trends within each period. An extraordinarily strong chemisorption is found for the O atom, 8.8 eV/adatom. On the basis of the calculated electronic structures, a concerted-coupling model for the chemisorption is proposed, in which two different types of adatom–substrate interactions work together to provide the obtained strong chemisorption: (i) adatom–TiSR and (ii) adatom–CSR's. This model is used to successfully describe the essential features of the calculated  $E_{\text{ads}}$  trends. The fundamental nature of this model, based on the Newns-Anderson model, should make it apt for general application to transition-metal carbides and nitrides, and for predictive purposes in technological applications, like cutting-tool multilayer coatings and MAX phases.

## I. INTRODUCTION

Titanium carbide (TiC) is an intriguing material. Like other early transition-metal carbides (TMC) and nitrides (TMN), it is characterized by a combination of properties that are traditionally assigned to two completely different types of materials: ceramics and metals. It possesses the physical properties (extreme hardness, high melting point, outstanding wear resistance, *etc.*) typical of ceramic materials, such as  $\text{Al}_2\text{O}_3$ , but exhibits at the same time electric and heat conductivities comparable to those of pure transition metals.<sup>1</sup> Such a behavior originates from a unique combination of covalency, ionicity, and metallicity.<sup>2</sup>

TMC's and TMN's, and in particular TiC, are often used or suggested for use in applications where their interaction with the environment (*e.g.*, growth, reactivity, tribology) is a crucial factor. Examples are: coating materials on, *e.g.*, cemented-carbide cutting tools,<sup>3</sup> microelectromechanical systems (MEMS),<sup>4</sup> fusion-reactor walls,<sup>5</sup> biocompatible materials,<sup>6</sup> and in space applications;<sup>7</sup> substrate or stabilizing interlayer material in recording heads,<sup>8</sup> for deposited diamond films,<sup>9</sup> in electronics,<sup>10</sup> and for the growth of carbidic nanostructures.<sup>11</sup> They have been suggested as good catalyst materials.<sup>12</sup> Also, they are one of the components in the MAX phases (such as  $\text{Ti}_3\text{SiC}_2$  and  $\text{Ti}_3\text{AlC}_2$ ), which are technologically interesting due to their unique combination of hardness and plasticity, properties that arise from the interaction between the layers of the  $\text{M}_6\text{X}$  (for example,  $\text{Ti}_6\text{C}$ ) octahedra and of the A component (such as Si or Al) that make up their structures.<sup>13</sup>

In the interaction of a material with its environment, chemisorption is the first step. Thus, a proper description of this interaction calls for an understanding of the

chemisorption properties and of the mechanisms behind them. This study focuses on TiC, since long considered a prototype for the early TMC's and TMN's, and on its (111) surface, which, although metastable, has shown to be the most reactive low-index surface of the early TMC's<sup>14</sup> and a frequently occurring surface in the above-mentioned applications.

So far, studies on the adsorption properties on the early TMC's have focused on the nonpolar and energetically favored (001) surface. For the polar and reactive (111) surface, information is more limited. Studies of H and O monolayers on the (111) surface of TiC and of other TMC's and TMN's, as well as of the clean-surface electronic structures, have been published.<sup>15,16,17,18,19,20,21,22,23,24,25,26,27,28</sup> However, to our knowledge, little has been done on the systematics of the chemisorption and in particular on connecting these findings into a general model, in which adsorption of other species is taken into account. Indeed, a desirable goal is to obtain a descriptive and predictive model for the nature of the interaction between adsorbate and substrate.

For these reasons, we perform an extensive theoretical investigation of atomic adsorption on the TiC(111) surface, based on quantum-mechanical first-principles calculations within the density-functional theory (DFT).<sup>29</sup> In order to understand the nature of the chemisorption, we perform a trend study, in which adsorption of H, of the second-period elements B, C, N, O, and F, and of the third-period elements Al, Si, P, S, and Cl are considered. For comparison, O adsorption on TiC(001) is also considered. In addition, in order to connect our results to the available experimental results, calculations on a full ( $1 \times 1$ ) monolayer of O on TiC(111) are performed and the results compared to the case of atomic adsorp-

tion. Also, the atomic and electronic structures of bulk TiC and of the clean TiC(111) and TiC(001) surfaces are studied in detail.

In this way, the nature of chemisorption is understood through detailed analyses of the changes in surface electronic structure upon adsorption and a model, describing the nature of the adatom–substrate interactions, is presented. By correlating the trends in calculated adsorption energies  $E_{\text{ads}}$  with the trends in calculated electronic structures for the different adatoms, indications about how  $E_{\text{ads}}$  depends on the adatom–TiC(111) interaction are thus obtained.

The organization of this paper is as follows. In Sec. II, the DFT computational method used is presented, including details of accuracy and convergence tests. Various densities of states (DOS) and other key tools for the analysis of our calculated electronic structures are defined. In Sec. III, the results from our calculations are presented and analyzed. Section III.A presents the results for bulk TiC, with detailed emphasis on the electronic structure. Earlier published results are confirmed. However, more details are given, in particular on the existence of direct  $Cp$ – $Cp$  bonding states in the lower part of the upper valence band (UVB) of TiC. Section III.B describes the results for the clean TiC(111) and (001) surfaces, including: surface relaxations, surface energetics, and electronic structures. Particular emphasis is given to the characterization of the surface electronic structures, with detailed descriptions of how they change compared to the bulk. Section III.C gives the results for the atomic adsorption on TiC(111) and (001), first describing in detail the calculated energetics, atomic structures (Sec. III.C.1), and electronic structures (Sec. III.C.2), and thereafter analyzing the obtained electronic-structure information (Sec. III.C.3). The systematics of the calculated electronic structures are used to formulate a “concerted-coupling” model, describing the nature of the interaction between the adsorbate atoms and the TiC(111) surface. Section III.D presents the results for full ( $1 \times 1$ ) monolayer coverage of O on TiC(111), including: energetics, atomic and electronic structures, and an analysis of the applicability of our concerted-coupling model to the case of full monolayer adsorption. In Sec. IV, we relate our electronic-structure results to the calculated trends in adsorption energies and discuss how our concerted-coupling model can be used in a qualitative way to understand the calculated trends in adsorption energy. In Sec. V, the main conclusions from the paper are briefly summarized.

## II. COMPUTATIONAL METHOD

The calculations are performed with the DFT plane-wave pseudopotential code `dacapo` 1.30.<sup>30</sup> The generalized-gradient approximation (GGA) of Perdew-Wang 1991 (PW91)<sup>31</sup> is used for exchange and correlation. The atomic nuclei and core electrons are de-

scribed with Vanderbilt ultrasoft pseudopotentials<sup>32</sup> and the Brillouin zone (BZ) is sampled with the Monkhorst-Pack scheme.<sup>33</sup> Slab geometry and periodic boundary conditions are employed and the potential discontinuity in the vacuum region thus arising from the lack of slab mirror symmetry is corrected for.<sup>34</sup> Full atomic relaxations within the given lattice parameters are performed using a BFGS quasi-Newton method, as implemented by Bengtsson.<sup>35</sup> On each considered system, the relaxation is performed until the sum of the remaining forces on all relaxed atoms in the unit cell is less than  $0.05 \text{ eV}/\text{\AA}$ , which corresponds to remaining forces on each individual atom of less than  $0.01 \text{ eV}/\text{\AA}$ .

The method and the Ti, C, O, and Al pseudopotentials have previously been shown to yield successful results for alumina bulk and surface structures,<sup>36,37</sup> as well as for TiC/Co interface studies.<sup>38</sup> The pseudopotential for B has been successfully employed to describe the binding in boron nitride.<sup>39</sup> The accuracy of the other pseudopotentials used in our calculations is tested by calculating the atomization energies of  $\text{H}_2$ ,  $\text{N}_2$ ,  $\text{F}_2$ ,  $\text{P}_2$ ,  $\text{S}_2$ , and  $\text{Cl}_2$  and the lattice constant and binding energy of bulk Si and comparing these results to the experimental values and to the results from similar calculations.

The electronic structures of the considered systems are analyzed by studying different types of local densities of states (LDOS), obtained from the calculated Kohn-Sham (KS) wavefunctions  $\Psi_n$  and energy eigenvalues  $E_n$ : (i) atom- and/or orbital-projected densities of states [LDOS( $E$ )] are obtained by projecting the KS wavefunctions onto the individual atomic orbitals and plotted as functions of the energy relative to the Fermi level,  $E - E_F$ ; (ii) the total density of states in real space, around a specific energy value, [DOS( $\mathbf{r}$ ,  $E$ )] is obtained by plotting  $|\Psi_n(\mathbf{r})|^2$ , integrated over the whole BZ, for the value of the band index  $n$  that corresponds to the KS energy  $E_n$  close to  $E$ . Also, band-structure plots are obtained by calculating the eigenvalues at  $\mathbf{k}$  points located along the BZ symmetry lines. These plots are analyzed in detail by plotting  $|\Psi_{n\mathbf{k}}(\mathbf{r})|^2$  in three-dimensional real space for the  $\mathbf{k}$  points located along the BZ symmetry lines.

In addition, a measure of the localization of charge around individual atoms is obtained from the calculated DFT charge density by using the “atoms-in-molecule”-method of Bader.<sup>40</sup> The algorithm of Ref. 41 is used. In these calculations, the charge density is sampled on a grid with grid-point separation of approximately  $0.07 \text{ \AA}$ . Also, the total-electron distribution in real space is analyzed by plotting the differences between the electronic densities calculated for the considered systems and those calculated for the systems composed of the corresponding free atoms.

For the calculations on bulk TiC (Sec. III.A), a plane-wave cutoff of 350 eV and a  $6 \times 6 \times 6$   $\mathbf{k}$ -point sampling are used. This has previously been shown to yield a good accuracy for bulk TiC.<sup>38</sup>

For the calculations on the clean TiC(111) surface (Sec. III.B), a 450 eV cutoff and a  $6 \times 6 \times 1$   $\mathbf{k}$ -point sampling

are used. The TiC structure is composed of Ti and C layers that alternate in the  $[111]$  direction (see Sec. III.B). In this paper, we define a “TiC bilayer” as the unit composed of one Ti and one C (111) atomic layer. Our calculations on the clean TiC(111) surface are performed on slabs composed of up to 15 such TiC bilayers. All considered slabs are stoichiometric, that is, they are composed of equal amounts of Ti and C atoms. Therefore, one side of the (111) slabs is terminated by a C layer, while the other side is terminated by a Ti layer. Because of this, only the “cleavage energy”  $E_{\text{cleav}}$ , that is, the sum of the C-terminated and Ti-terminated surface energies, can be calculated:

$$E_{\text{cleav}} = E_{\text{cell}}(n) - nE_{\text{b}},$$

where  $E_{\text{cell}}(n)$  is the total energy of a slab with  $n$  TiC bilayers, as obtained from our DFT calculations, and

$$E_{\text{b}} = E_{\text{cell}}(n) - E_{\text{cell}}(n-1)$$

is the bulk energy of one TiC bilayer.<sup>42,43,44</sup> The cleavage energy corresponds to the energetical cost of cleaving the infinite TiC crystal into two semi-infinite crystals. Convergence of  $E_{\text{b}}$  is obtained for  $n \geq 4$ , disregarding quantum-size oscillations,<sup>44,45</sup> which make the calculated cleavage energy values vary by at most  $\pm 0.3$  J/m<sup>2</sup>. The thickness of the vacuum region is 8.75 Å, corresponding to the thickness of four TiC bilayers. Increasing the cutoff energy from 350 eV to 450 eV and/or the vacuum thickness from four to six TiC bilayers changes the calculated  $E_{\text{cleav}}$  value for the unrelaxed slab by less than 0.1 J/m<sup>2</sup>.

For the adatom calculations on TiC(111) (Sec. III.C), a slab composed of four TiC bilayers is used. In order to be able to compare our results with those from our study of the formation of thin films of  $\alpha$ - and  $\kappa$ -Al<sub>2</sub>O<sub>3</sub> on TiC(111),<sup>46</sup> orthogonal surface lattice parameters, resembling the structure of the  $\kappa$ -Al<sub>2</sub>O<sub>3</sub>(001)/(00 $\bar{1}$ ) surface,<sup>37</sup> are used in these calculations (see Fig. 1). Each atomic Ti/C layer is thus composed of six atoms in a  $(2 \times 3)$  geometry. The adatom and the top three TiC bilayers are allowed to relax in all directions. A  $4 \times 2 \times 1$   $\mathbf{k}$ -point sampling, a 400 eV cutoff energy, and a vacuum thickness of at least 9.6 Å are used. The adsorption energy of the adatom is calculated as

$$E_{\text{ads}} = E_{\text{slab+adatom}} - E_{\text{slab}} - E_{\text{atom}},$$

where  $E_{\text{slab+adatom}}$  is the calculated energy of the fully relaxed TiC slab with the adatom,  $E_{\text{slab}}$  is the energy of the relaxed clean TiC slab, and  $E_{\text{atom}}$  is the energy of the free adatom. All values are calculated with the same supercell size, plane-wave cutoff energy, and  $\mathbf{k}$ -point sampling. The accuracy is tested by considering the system with strongest adsorption energy, an O adatom adsorbed in the fcc site, and repeating its relaxation with an  $8 \times 4 \times 1$   $\mathbf{k}$ -point sampling, a 700 eV plane-wave cutoff, a 20.6 Å vacuum thickness, and a slab thickness of seven



FIG. 1: Surface unit cell used for the adsorbate calculations on TiC(111). The  $(4 \times 3)$  unit cell used for the fcc adatoms is marked by the lines and the shaded atoms. Large lighter circles are Ti atoms, small darker circles are C atoms, and the small black circle is the adsorbed atom. The present picture shows the relaxed structure of an adsorbed O atom in the fcc site. The  $(2 \times 3)$  unit cell, also used in the calculations (see text for details), is also shown (dashed arrow).

TiC bilayers, respectively. None of these changes produces a change in calculated adsorption energy of more than  $\pm 0.05$  eV/adatom.

In addition, in order to test any presence of adatom–adatom interactions, the relaxation of all adatoms in fcc site is repeated using supercells in which each atomic layer is composed of 12 atoms in a  $(4 \times 3)$  geometry (Fig. 1). A  $2 \times 2 \times 1$   $\mathbf{k}$ -point sampling is used. Again, no change in adsorption energy larger than 0.05 eV/adatom is obtained. However, for the adatoms with large radii (atomic or ionic, depending on the degree of ionicity of the adsorbate–substrate bond, see Sec. III.C.2) (B, F, Al, Si, and Cl), slightly asymmetric adsorbate–substrate bond lengths are found after relaxation of the  $(2 \times 3)$  supercell. Also, evidence for adatom–adatom interactions are found in the calculated DOS’s for these adatoms. Therefore, all results in this paper on the atomic adsorption in the fcc site on TiC(111) are those obtained from the  $(4 \times 3)$  supercell.

For the calculations on the clean and the O-adsorbed TiC(001) surfaces (Secs. III.B and III.C), a slab composed of five atomic layers is used. Each TiC(001) atomic layer consists of equal amounts of Ti and C atoms (see Sec. III.B). In order to allow sufficient distance between the adsorbed O adatoms, the surface cell dimensions are chosen such that each layer is composed of 16 atoms (eight Ti and eight C) in a  $(4 \times 4)$  geometry. A 450 eV

cutoff, a  $4 \times 4 \times 1$   $\mathbf{k}$ -point sampling, and a vacuum thickness of at least 10.9 Å are used. Since the two surfaces of a TiC(001) slab are equivalent, the calculated (001) cleavage energy corresponds to twice the (001) surface energy.

Finally, the calculations on a full O( $1 \times 1$ ) monolayer on TiC(111) (Sec. III.D) are performed using both a slab with 15 TiC bilayers (and one atom per atomic layer) and a slab with 4 TiC bilayers [and six atoms per layer in a ( $2 \times 3$ ) geometry]. The same parameters are used as for the above-described 15-bilayer and ( $2 \times 3$ ) 4-bilayer slabs, respectively. Between these two slab, the calculated interlayer relaxations of the O monolayer and of the top two TiC bilayers differ by less than 0.02 Å and the calculated adsorption energies differ by less than 0.1 eV/adatom.

### III. RESULTS AND ANALYSIS

#### A. Bulk TiC

##### 1. Atomic Structure

Bulk TiC adopts the NaCl structure. The lattice parameter obtained from our calculation (4.332 Å) is very close to the experimental value (4.330 Å).<sup>47</sup> Along the [111] direction, the structure is composed of alternating Ti and C layers, stacked in an *ABC* sequence (see Sec. III.B), with calculated interlayer distance of 1.251 Å, Ti–C bond length of 2.166 Å, and Ti–Ti and C–C distances within each (111) layer of 3.063 Å.

##### 2. Electronic Structure

The nature of the bonding in bulk TiC and other TMC's and TMN's has been extensively studied over many years, both experimentally and theoretically.<sup>2,47,48,49,50,51,52,53</sup> The common viewpoint that emerges from these studies is that the bonding in several TMC's and TMN's is dominated by strong, directional, covalent M–X bonds (M: metal atom, X: C or N), which account for the high hardness of these compounds.<sup>54</sup> At the same time, a transfer of electrons from M to X takes place, implying a certain degree of ionic bonding. Further, the DOS does not vanish at the Fermi energy ( $E_F$ ), giving the compounds a metallic character. Thus, the bonding in TiC is mainly due to covalent Ti–C bonds, in which a certain degree of ionicity (electron transfer from Ti to C) can be detected, combined with a smaller amount of metallic Ti–Ti bonds. Most previous studies have excluded the presence of direct C–C interactions *a priori*. However, more recently, a COOP (crystal orbital overlap populations) analysis has pointed out the presence of bonding and antibonding C–C interactions in the lower

and upper parts of the TiC upper valence band (UVB), respectively.<sup>55</sup>

In the following, we present our results on the electronic structure of bulk TiC. The presence of ionic-covalent Ti–C bonds and of metallic Ti–Ti bonds is confirmed and analyzed in detail. In addition, our analysis clearly shows that bonding C–C states are present in the lower part of the UVB. Our subsequent analysis of the adsorption on the TiC(111) surface (Sec. III.C.3) shows this to be important for the formulation of a model for adsorption on TiC. Therefore, we pursue in this and the following subsection detailed analyses of both the previously characterized Ti–C and Ti–Ti states and the so far largely neglected C–C states.

Our calculated band structure and DOS( $E$ ) for bulk TiC are shown in Figs. 2 and 3. The lower valence band (LVB), peaked at 9.5 eV below  $E_F$ , is dominated by C  $2s$  states, with only small contributions from Ti. The upper valence band (UVB) is mainly composed of C  $2p$  and Ti  $3d$  states and extends above  $-6.1$  eV, with a major peak at  $-2.5$  eV and smaller peaks at  $-4.0$  and  $-1.7$  eV (all energies here and in the following are given relative to  $E_F$ ). No C  $sp$  hybridization is detected. The main contribution to the UVB comes from the C  $2p$  orbitals, indicating the partially ionic nature of the Ti–C bond. However, the large overlap of Ti and C states, in particular around and above the main UVB peak, demonstrates a strong covalent character of the bond. The UVB and the conduction band (CB), on each side of  $E_F$ , form a continuum, with a wide, nonzero but deep, minimum in the DOS around  $E_F$ . The lowest value of the DOS is approximately 0.21 states/(eV·TiC-unit), in good agreement with previous theoretical and experimental results.<sup>48,52</sup> This confirms the metallic character of the crystal. The CB has mainly Ti  $3d$  character, with a smaller C  $2p$  contribution, which again indicates the partially ionic character of the Ti–C bond. Still, an overlap of the Ti and C states can be seen, which is consistent with the view that the CB arises mainly from the antibonding states of the Ti–C covalent interaction.

Due to the octahedral symmetry around the Ti site in bulk TiC, the Ti  $3d$  electrons redistribute into orbitals of  $e_g$  (*i.e.*,  $x^2 - y^2$  and  $z^2$ ) and  $t_{2g}$  (*i.e.*,  $xy$ ,  $yz$ , and  $zx$ ) symmetries.<sup>2,47,50,51,52</sup> The  $e_g$  orbitals point toward the nearest C-atom sites, while the  $t_{2g}$  orbitals point toward the tetrahedral holes in the fcc Ti-atom network.<sup>2,47</sup> Our calculated LDOS, projected onto Ti  $e_g$  and  $t_{2g}$  orbitals (Fig. 3), shows a dominating  $e_g$  character of the UVB. On the other hand, both the states around  $E_F$  and in the CB are dominated by  $t_{2g}$  orbitals.

These results agree well with those obtained from the previous studies on the bonding nature of bulk TiC.<sup>2,47,48,49,50,51,52,53</sup> According to them, the UVB is dominated by bonding Ti–C  $\sigma$  states between Ti  $3d(e_g)$  and C  $2p$  orbitals ( $pd\sigma$ ), with contributions from Ti–Ti  $\sigma$  states between the Ti  $3d(t_{2g})$  orbitals ( $dd\sigma$ ) and from Ti–C  $\pi$  states between Ti  $3d(t_{2g})$  and C  $2p$  orbitals ( $pd\pi$ ).

However, our results show also that (i) the Ti DOS is

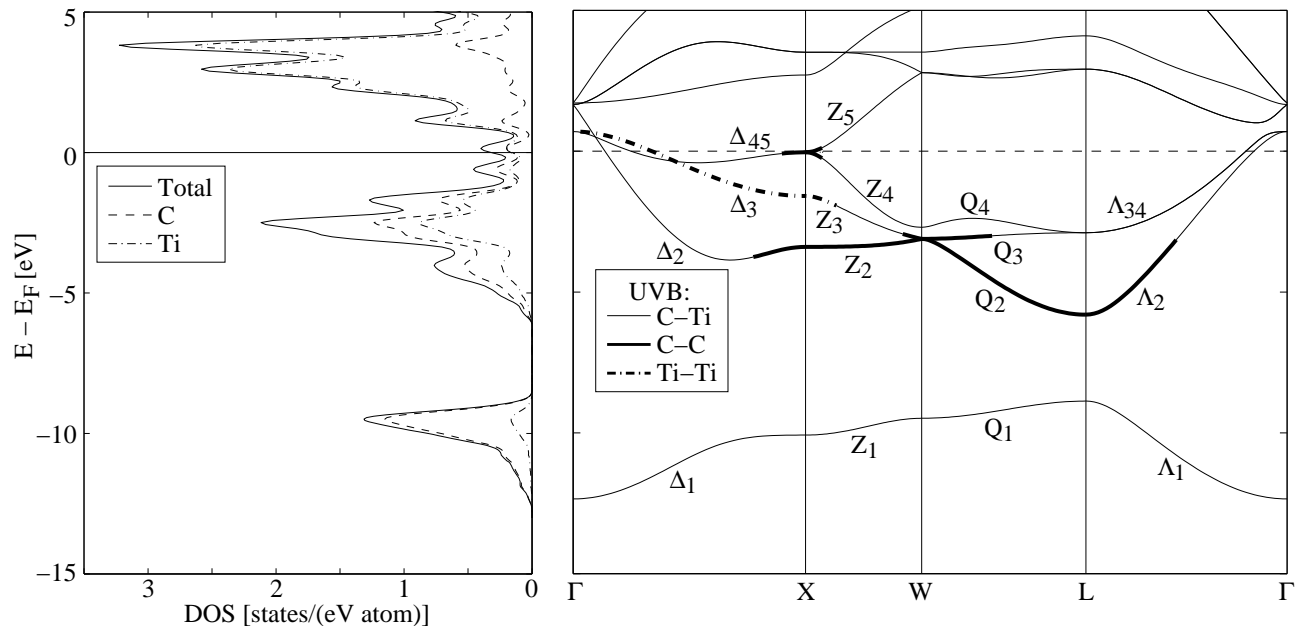


FIG. 2: Calculated band structure (right) and total and atom-projected DOS( $E$ ) (left) for bulk TiC. The high-symmetry points in the Brillouin zone are  $\Gamma = (0, 0, 0)$ ,  $X = \frac{2\pi}{a}(0, 1, 0)$ ,  $W = \frac{2\pi}{a}(\frac{1}{2}, 1, 0)$ , and  $L = \frac{2\pi}{a}(\frac{1}{2}, \frac{1}{2}, \frac{1}{2})$ , where  $a$  is the primitive-lattice parameter of bulk TiC. The band-structure plot shows also which parts of the upper valence band (UVB) correspond to C–Ti, C–C, and Ti–Ti bonding states, respectively, according to our state-resolved analysis of the DOS (described in the text and illustrated in Fig. 4).

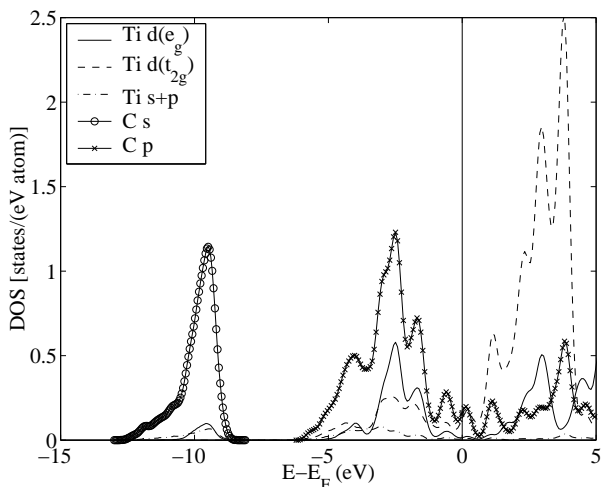


FIG. 3: Calculated DOS( $E$ ) for bulk TiC, projected onto Ti  $d$  valence orbitals with  $e_g$  and  $t_{2g}$  symmetry, respectively, onto Ti  $s + p$  valence orbitals, and onto C  $s$  and  $p$  valence orbitals, respectively.

very weak in the energetical region below the main UVB peak, (ii) no particular symmetry preference [ $s$ ,  $p$ ,  $d(e_g)$ , or  $d(t_{2g})$ ] can be detected for the Ti states in this region, and (iii) C states are also present around  $E_F$ .

In order to further investigate these issues, we examine real-space, three-dimensional, plots of  $|\Psi_{n\mathbf{k}}(\mathbf{r})|^2$  (see Sec. II) for a number of states  $n\mathbf{k}$  along all the valence bands

of the TiC band structure. This analysis confirms the claims of previous studies, regarding the Ti–C and Ti–Ti bonds in bulk TiC. However, it also gives more detailed information on the types of bonding states present in the UVB and on where they are located in the band structure: (i) Ti–C bonds are mainly found along  $\Delta_2$  ( $pd\sigma$  bonds),  $\Delta_{45}$  ( $pd\pi$ ),  $Z_4$  ( $pd\sigma$ ),  $Q_3$  and  $Q_4$  ( $pd\sigma$  and  $pd\pi$ ), and  $\Lambda_{34}$  ( $pd\pi$ ) [Figs. 4(a) and (b) illustrate this by the  $pd\sigma$  and  $pd\pi$  bonds at the minimum energy point of  $\Delta_2$  and at the  $L_{34}$  point, respectively]; (ii) Ti–Ti  $dd\sigma$  bonds within the TiC{001} planes are found along the  $\Delta_3$  band and around the  $X_3$  point, as illustrated by the three-dimensional contour plot of  $|\Psi_{n\mathbf{k}}(\mathbf{r})|^2$  at the  $X_3$  point [Fig. 4(c)].

In addition, our analysis shows the clear presence of C–C bonding states, mainly in the lower part of the UVB: the states around the  $X_2$ ,  $X_{45}$ ,  $W_{23}$ , and  $L_2$  points, and along the  $Z_2$ ,  $Q_2$ , and the lower part of the  $\Lambda_2$  symmetry lines consist almost exclusively of C–C bonding states (Fig. 2). Of these states, only those along  $Q_2$  and the lower part of  $\Lambda_2$  contain some amount of Ti–C bonding states. These C–C bonding states are of both  $pp\pi$  (at  $X_2$ ,  $X_{45}$ , and along  $Z_2$  and the lower part of  $Q_2$  and of  $\Lambda_2$ ) and  $pp\sigma$  (at  $W_{23}$  and along the higher part of  $Q_2$ ) characters. Figures 4(e) and (d) illustrate this, showing  $|\Psi_{n\mathbf{k}}(\mathbf{r})|^2$  at  $L_2$  and at  $W_{23}$ , respectively. Thus, as already suggested by the low Ti LDOS in this region, the lower part of the TiC UVB is almost exclusively composed of bonding C–C states, with very small Ti–C con-



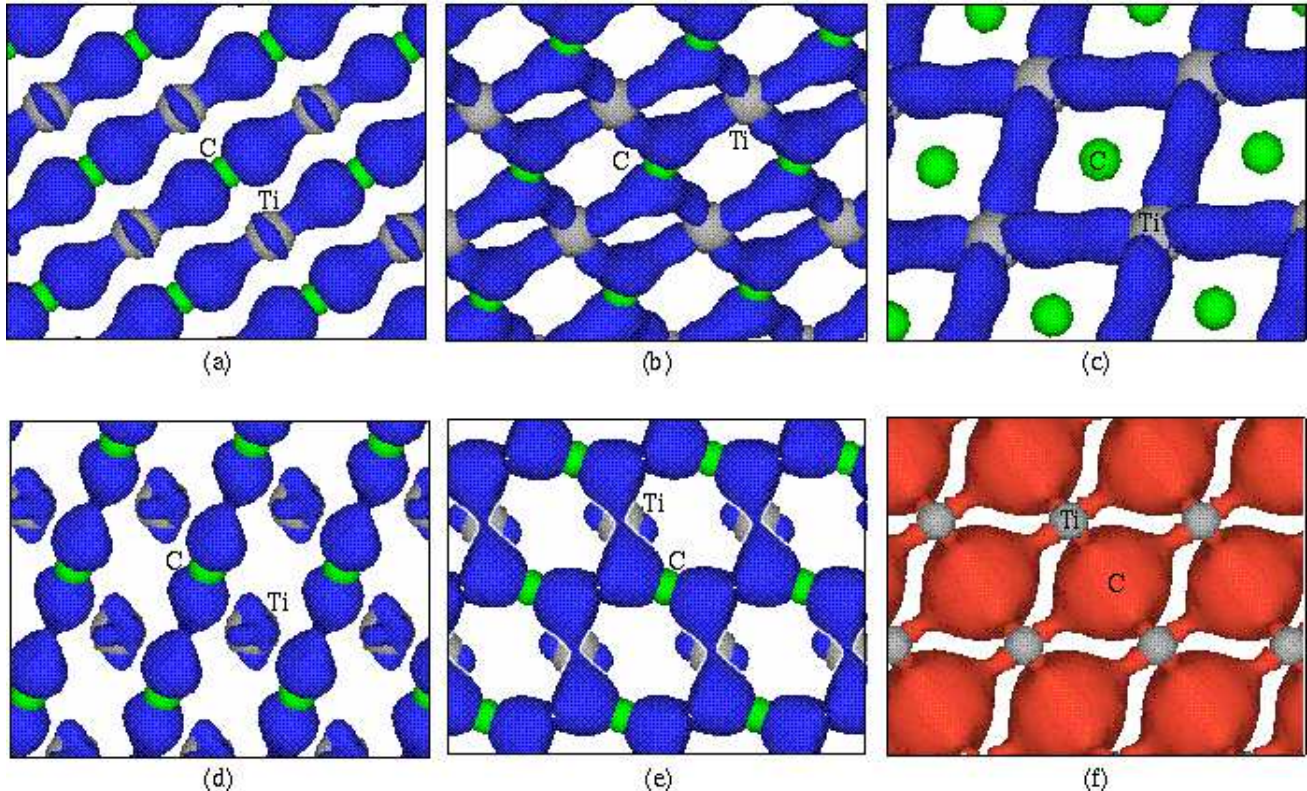


FIG. 4: (Color online). (a)–(e) Three-dimensional real-space contour plots of  $|\Psi_{n\mathbf{k}}(\mathbf{r})|^2$  in bulk TiC for the states  $n\mathbf{k}$  at: (a) the point of lowest energy of the  $\Delta_2$  band, showing Ti( $e_g$ )-C( $p$ )  $\sigma$  bonds; (b) the  $L_3$  point, showing Ti( $t_{2g}$ )-C( $p$ )  $\pi$  bonds; (c) the  $X_3$  point, showing Ti( $t_{2g}$ )-Ti( $t_{2g}$ )  $\sigma$  bonds; (d) the  $W_2$  point, showing C( $p$ )-C( $p$ )  $\sigma$  bonds; (e) the  $L_2$  point, showing C( $p$ )-C( $p$ )  $\pi$  bonds. (f) Three-dimensional contour plot of the difference between the total electron density in bulk TiC and the electron density of free Ti and C atoms. All subfigures are viewed perpendicular to the  $[111]$  direction, except (c), which shows a  $\{001\}$  plane. Larger (grey/lighter) balls are Ti atoms, smaller (green/darker) balls are C atoms. In subfigure (f) the C atoms are hidden inside the large electron clouds. Note that in subfigure (e), the Ti electron clouds lie behind and are not connected to the C-C electron clouds. The contour plots correspond to density values of (a)–(e) 0.17 electron states/ $\text{\AA}^3$  and (f) +0.02 electron states/ $\text{\AA}^3$ .

tributions.

Figure 4(f) shows the difference between the total electron density in bulk TiC and the electron density of free Ti and C atoms, that is, how the valence-electron distribution is changed by the formation of bonds in bulk TiC. The plot confirms the partially ionic character of the bond, with a clear charge transfer from the Ti to the C atoms (this is also confirmed by an analysis of the regions of negative charge-density difference). At the same time, it can be seen that the covalent interaction is dominated by the Ti-C  $\sigma$  bonds.

Thus, we can conclude that the main contribution to the cohesion of bulk TiC comes from the ionic-covalent Ti-C  $\sigma$  bonds (in agreement with previous studies), but that our state-resolved analysis of the electron density [Figs. 4(a)–(e)] shows that Ti-C  $\pi$ , Ti-Ti  $\sigma$ , C-C  $\sigma$ , and C-C  $\pi$  bonding states also are present in the UVB of bulk TiC, in different energy regions (Fig. 2): C-C bonding states are present in the lower part of the UVB (between approximately  $-5.8$  and  $-3.1$  eV); Ti-C bonding states

are present from  $-3.9$  eV all the way up to  $E_F$ ; Ti-Ti bonding states are present between approximately  $-1.6$  and  $+0.7$  eV. Some C-C bonding states are also found around the  $X_{45}$  point, at  $E_F$ . As will be seen later, knowledge about the presence and energetical location of these different states is important for an understanding of the mechanism behind atomic adsorption on TiC.

Finally, we estimate the ionic character of bulk TiC by calculating the charge around each atom with the “atoms-in-molecule” method of Bader (see Sec. II). This yields a charge transfer of 1.5 electrons from Ti to C, in excellent agreement with the results from Mulliken population analyses of other calculations.<sup>15,16</sup>

## B. Clean TiC(111) and TiC(001) surfaces

The TiC(111) surface has been characterized, experimentally and theoretically, to be Ti( $1 \times 1$ ) terminated [Figs. 5(a-b)].<sup>17,18,19,20</sup> Due to the partial ionicity and

NaCl structure of TiC, its (111) surface is polar, that is, it is energetically unstable due to the long-range electric field caused by the nonzero dipole moment, perpendicular to the surface, of the TiC bilayer.<sup>56</sup> However, previous calculations have shown that this polarity is cancelled by a lowering of the ionic charge at the surface by approximately 50%, due to the downward shift of the Ti antibonding CB LDOS at the surface.<sup>15,16</sup> Experiments have indeed shown the presence of a Ti-centered surface resonance (TiSR) just below  $E_F$ .<sup>18,19,21,22,76</sup>

In contrast, the TiC(001) surface is nonpolar, being composed of equal amounts of positively charged Ti atoms and negatively charged C atoms [see Fig. 5(c)]. Neither charge transfer nor surface resonance (SR) at  $E_F$  have been reported for this surface.

In the following, we present our results from DFT calculations on these two surfaces. First, the relaxed atomic geometries and cleavage energies are presented and compared with previous results. Then, we focus on the electronic structures of the two surfaces, in particular the (111) surface, describing in detail how they differ from the bulk electronic structure. These results are in a general agreement with the few earlier studies.<sup>15,16,17,18,19,21,22</sup> However, our analyses provide a much greater resolution of the surface electron-structure features and show a so far neglected wealth of different SR's, in particular on the (111) surface. Knowledge about the presence and nature of these SR's is essential for the subsequent analysis of the electronic structures of the atomic adsorbates.

### 1. Geometry and Energetics

For the (111) surface, our calculations on the 15-bilayer slab (see Sec. II) yield relaxations of the top six interlayer distances of  $-19.2\%$ ,  $+11.0\%$ ,  $-5.8\%$ ,  $+0.6\%$ ,  $-0.7\%$ , and  $-1.0\%$  [Fig. 5(b)]. The large first-layer relaxation is in qualitative agreement with the one observed by Aono *et al.*<sup>17</sup> by impact-collision ion scattering spectroscopy (ICISS) ( $-30\%$ ), and all values agree well with those from the tight-binding calculation of Tan *et al.*<sup>20</sup> The sum of the calculated top two interlayer distances (2.40 Å) agrees also very well with the value 2.3 Å from the STM investigation by Ahn *et al.*<sup>23</sup> The calculated relaxed bond length between the surface Ti and C atoms is 2.041 Å, which corresponds to a 6% decrease from the bulk value of 2.166 Å.

For the (001) surface, our calculations yield the ruffled relaxation described in the literature, with the C atoms relaxing outwards and the Ti atoms inwards.<sup>57,58</sup> This results in a perpendicular C–Ti distance of 0.11 Å in the surface layer, in excellent agreement with recent experimental results ( $0.13 \pm 0.04$  Å).<sup>58</sup> Our relaxed perpendicular distances between the surface-layer Ti and subsurface-layer C (2.08 Å) and between C and Ti within the subsurface layer (0.03 Å) [see Fig. 5(d)] are also in good agreement with the experimental results ( $2.11 \pm 0.04$

Å and  $0.01 \pm 0.04$  Å, respectively).<sup>58</sup>

For the cleavage energies, *i.e.*, the energy required to cleave the infinite crystal along a chosen plane (as defined in Sec. II), we obtain  $E_{\text{cleav}} = 11.74$  J/m<sup>2</sup> for the unrelaxed (111) surface and  $E_{\text{cleav}} = 11.43$  J/m<sup>2</sup> after relaxation of only the Ti-terminated side of the (111) slab. Since the (111) slab is stoichiometric, these values correspond to the sum of the surface energies of the Ti- and C-terminated TiC(111) surfaces, respectively (see Sec. II). However, the calculated energy gain of the relaxation, 0.31 J/m<sup>2</sup>, corresponds to the surface-energy gain of relaxing only the TiC(111)-Ti surface. For the (001) surface, a value of  $E_{\text{cleav}} = 3.52$  J/m<sup>2</sup> is obtained after relaxation. Since the (001) slab is mirror symmetric with respect to the (001) plane,  $E_{\text{cleav}}$  corresponds to twice the surface energy for this surface.

These values of  $E_{\text{cleav}}$  agree well with the results from previous DFT calculations performed with the VASP code:<sup>59</sup>  $E_{\text{cleav}} = 3.46$  J/m<sup>2</sup> for the relaxed TiC(001), 7.56 J/m<sup>2</sup> for the relaxed TiC(011), and 11.26 J/m<sup>2</sup> for the relaxed TiC(111).<sup>60</sup> Thus, we see that the energetical order of the three low-index surfaces of TiC is (001) < (110) < (111). The lower stability of (111), with respect to (001), is expected, since the polar nature of the (111) surface should decrease its stability.<sup>56</sup>

### 2. Electronic Structure: TiC(111)

(a) *Fermi-level surface resonance.* The calculated DOS( $E$ ) for the relaxed TiC(111) surface is shown in Figs. 6 and 7. The bulk DOS (Fig. 2) is recovered in the third TiC surface bilayer. The top two bilayers are characterized by a strong SR, peaked right beneath  $E_F$ , of almost exclusively Ti  $3d$  character (TiSR). The energetical position and Ti  $d$  character of the TiSR are in good agreement with the results from previous experimental and theoretical studies.<sup>15,16,19,21,22</sup> In addition, our orbital projection of the DOS (Fig. 7) shows that the TiSR can be decomposed into (i) a main peak at  $-0.1$  eV that consists of mainly  $d_{(xz,yz)}$  and  $d_{(xy,x^2-y^2)}$  orbitals (the  $z$  axis is here and in the following taken perpendicular to the surface) and (ii) a high-energy shoulder, above  $E_F$ , that consists almost exclusively of  $d_{(xz,yz)}$  orbitals. The highest density of  $d_{(xz,yz)}$  orbitals is found at  $+0.3$  eV.

The real-space shape of the TiSR (Fig. 8) reveals this mixed  $d_{(xz,yz)} + d_{(xy,x^2-y^2)}$  symmetry: the electron distribution protrudes into the vacuum, while binding to neighboring surface Ti atoms. However, the TiSR electron density is not homogeneously distributed within the surface plane: the TiSR avoids the regions with C atoms directly underneath, that is, the hcp adsorption sites (see Sec. III.C.1). Therefore, the surface Ti–Ti bonds are present only in the regions corresponding to the fcc adsorption sites. Also, similar plots show that, for lower DOS values, the TiSR density couples to states centered around Ti atoms lying deeper into the bulk, motivating our choice of calling these states SR's rather than surface

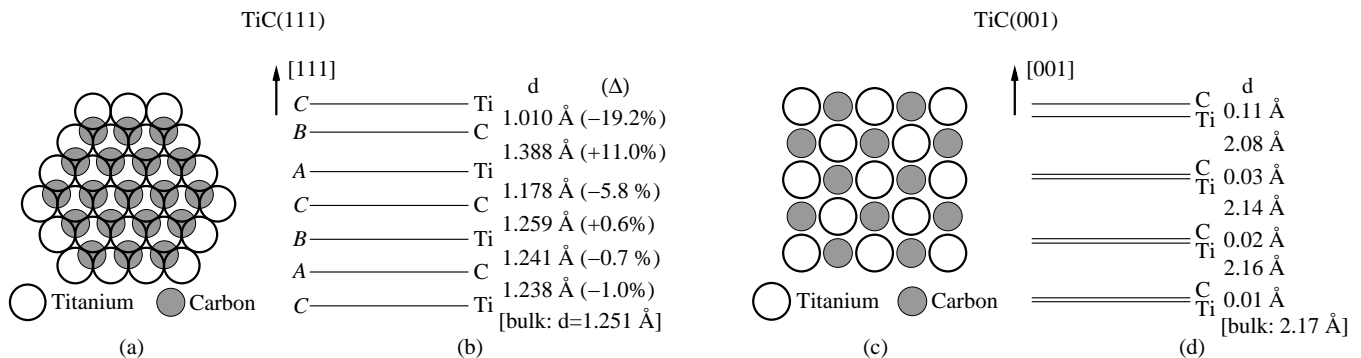


FIG. 5: Surface structure of TiC(111) and (001): (a) top view of the two atomic top layers of TiC(111); (b) the top seven atomic surface layers of TiC(111), seen perpendicularly to [111], showing the  $ABC$  stacking of alternating Ti and C layers and the interlayer relaxations, in absolute values ( $d$ ) and relative to the bulk distance ( $\Delta$ ), as calculated with our 15-bilayer slab (see Sec. II); (c) top view of the surface atomic layer of TiC(001); (d) the top four surface layers of TiC(001), seen perpendicularly to [001], showing the rumpled relaxation of this surface, as obtained from our calculations.

states.

This spatial extent of the TiSR agrees with the one suggested by Aono *et al.*<sup>17</sup> and can be understood by considering the TiSR as containing dangling bonds that result from the breakage of the iono-covalent Ti–C bonds that cross the (111) cleavage plane. The breakage of these bonds causes the corresponding empty, antibonding, Ti-centered states of the bulk CB to collapse into more atomic-like orbitals, thus lowering their energy. Therefore, the TiSR contains unsaturated Ti orbitals that point toward the sites that were previously occupied by the C atoms, that is, the surface fcc sites [Fig. 8(b)]. At the same time, the TiSR can also be expected to contain broken Ti–Ti  $dd\sigma$  bonds [Fig. 4(c)] that rearrange into new Ti–Ti hybridizations within the surface (111) plane.

As noted above, previous calculations have led to the argument that the presence of a partially-filled TiSR causes an electron transfer to the surface Ti atoms and a resulting decrease in their ionicity of approximately 50%, compared to the bulk.<sup>15,16</sup> Since TiC is partially ionic, the TiC(111) surface is polar and should therefore be unstable, due to the presence of a macroscopic electric field caused by the nonzero perpendicular dipole moment of the TiC bilayer.<sup>56</sup> However, this field can be neutralized by inducing a surface charge that exactly cancels out the bulk macroscopic field. For the (111) surface of a crystal with the NaCl structure, such as TiC(111), this surface charge should be equal to 50% of the bulk ionicity.<sup>15</sup> Based on the above-mentioned calculations, it has been argued that the extra electronic states needed to accommodate this charge at the Ti-terminated surface are provided by the TiSR.<sup>15,16</sup>

A Bader analysis (see Sec. II) of the atomic charges in our TiC(111) slabs yields that (i) in the middle of the slabs, a charge transfer from Ti to C atoms of approximately 1.55 electrons/atom takes place (in good agreement with our bulk results, see Sec. III.A.2); (ii) close to the Ti-terminated (C-terminated) surface of the slab, there is a total net charge of approximately

$-0.8$  ( $+0.8$ )  $|e|/\text{atom}$ . Thus, approximately 0.8 electrons/atom are transferred from the C-terminated side to the Ti-terminated side of the slab. This amount corresponds to  $0.8/1.55 = 52\%$  of the ionicity in the middle of the slab, which is in excellent agreement with the previous results of a 50% reduction in surface ionicity.

However, a more detailed analysis of our Bader charges for the Ti-terminated surface shows that this surface charge is not located exclusively on the surface Ti atoms, but rather distributed among both Ti and C atoms of the top two TiC bilayers: the charge on the surface Ti atoms is  $+1.1 |e|/\text{atom}$ , that is, only  $\sim 0.45$  more electrons than on the bulk Ti atoms. The remaining extra surface electrons are located on the C atoms of the first TiC bilayer (0.25 electrons/atom) and on the Ti and C atoms of the second TiC bilayer (0.03 electrons/atom on both Ti and C). Thus, the extra electrons do not only give rise to a TiSR but also an increased ionicity of the surface C atoms, compared to the bulk. This is characteristic of electron-structure changes also around the surface-bilayer C atoms, a point that is pursued further in the next subsection.

Finally, it should be noted that the TiSR DOS peak is rather sharp, indicating a small dispersion and therefore a weak coupling between neighboring surface Ti atoms and with the bulk states at  $E_F$ . This is confirmed by our real-space plot of the TiSR (Fig. 8), which shows that the electron density is very weak in the surface fcc sites, compared to the Ti sites, but also by an analysis of the band structure around  $E_F$ , as calculated for a slab with four TiC bilayers (Fig. 9). Analysis of contour plots of  $|\Psi_{n\mathbf{k}}(\mathbf{r})|^2$  for a number of  $\mathbf{k}$  points along this band structure allows an identification of the states that show a strong localization around the surface Ti atoms. These states, marked with circles in Fig. 9, show that the TiSR lies at  $-0.5$  eV at  $\bar{\Gamma}$  and disperses upwards in both the  $\bar{\Gamma}\bar{M}$  and  $\bar{\Gamma}\bar{K}$  directions, crossing  $E_F$ . The dispersion is smaller than 1 eV. Both the direction and the strength of the dispersion agree qualitatively with previous theoret-



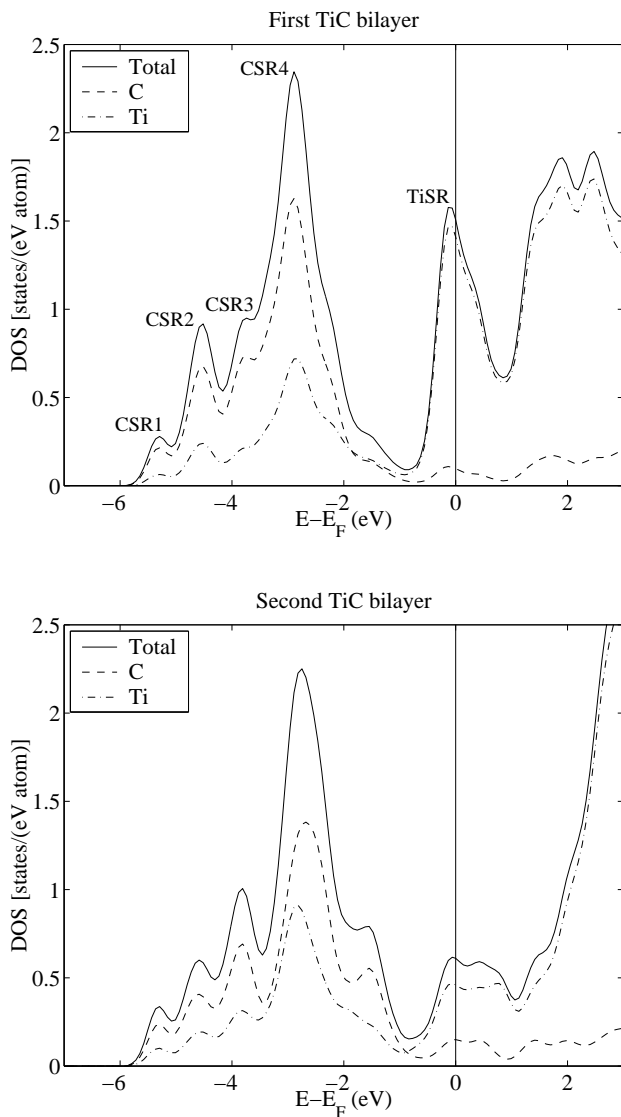


FIG. 6: Total and atom-projected  $\text{DOS}(E)$  for the top two TiC bilayers of the clean TiC(111) surface. In the surface-bilayer DOS, the four UVB peaks and the peak at  $E_F$  are identified as C-localized (CSR1–CSR4) and Ti-localized (TiSR) surface resonances, as described in the text.

ical results for TiC(111)<sup>16</sup> and with experimental results for the largely similar NbC(111) surface.<sup>24</sup>

(b) *UVB and LVB.* The UVB of the TiC(111) surface bilayer extends between  $-5.9$  and  $-0.7$  eV and is largely similar to the bulk UVB. However, a detailed analysis reveals a number of differences: (i) the position of the main peak lies at  $-2.9$  eV, that is,  $0.4$  eV lower than in the bulk UVB; (ii) the bulk-UVB high-energy peak (at  $-1.7$  eV) is strongly quenched; (iii) the bulk-UVB low-energy peak (at  $-4.0$  eV) is replaced by three peaks, at  $-3.7$ ,  $-4.5$ , and  $-5.3$  eV; (iv) the surface UVB DOS is more strongly localized around the C atoms than the bulk UVB DOS.

Our analysis of the  $\text{DOS}(\mathbf{r}, E)$  (see Sec. II) for all states

within the surface UVB shows that the surface UVB can be divided into three regions, according to the bonding nature of its states: (i) a high-energy region, between  $-1.7$  and  $-0.7$  eV, consisting of C–Ti bonding states with higher electron concentration around the Ti atoms; (ii) a middle region, between  $-3.3$  and  $-1.8$  eV, consisting of C–Ti bonding states with higher electron concentration around the C atoms; and (iii) a low-energy region, between  $-5.9$  and  $-3.3$  eV, consisting of primarily C–C bonding states, with some contribution from C–Ti interactions. The high-energy region corresponds to the quenched high-energy bulk peak, the middle region corresponds to the main peak, and the low-energy region corresponds to the three low-energy peaks.

The differences between the bulk and surface UVB DOS's can be understood in a way analogous to our discussion on the origin of the TiSR. The high-energy region of the bulk UVB is composed of bonding Ti–C states, with higher localization on the C atoms. Cleavage of the bulk structure to create the (111) surface breaks these Ti–C bonds and removes the corresponding C atoms. Therefore, these Ti–C bonding states collapse into more C-centered, atomic-like, states, which disappear as the corresponding C atoms are removed upon cleavage. This shows up in our surface DOS as a quenching of the bulk-UVB peak at  $-1.7$  eV.

Similarly, the formation of the surface causes the breakage of the C–C bonds present in the lower part of the bulk UVB (see Sec. III.A.2). The DOS changes in the low-energy UVB region can therefore be interpreted as evidence for the formation of C-centered dangling bonds or SR's (CSR's). Such an interpretation is corroborated by our calculated  $\text{DOS}(\mathbf{r}, E)$  for the energetical regions around each of the UVB peaks in the surface  $\text{DOS}(E)$  (illustrated by Fig. 10). A higher localization and different orbital symmetry of these states around the surface-bilayer C atoms is clearly visible. Also, at low values of the  $\text{DOS}(\mathbf{r}, E)$ , these states connect to the second-bilayer C-atom states, giving these states the status of SR's.

Finally, the higher localization of the surface UVB DOS around the C atoms, compared to the bulk, is further evidence for the higher ionicity of the surface-bilayer C atoms, already discussed above in conjunction with our surface Bader analysis. Our analysis above shows that this higher ionicity is caused by the presence of CSR's on these atoms.

The LVB of the TiC(111) surface is peaked at  $-9.9$  eV and is almost exclusively composed of C  $2s$  orbitals, like the bulk LVB. Again, we note a shift of  $0.4$  eV to lower energy, compared to the bulk LVB.

(c) *Total electron density.* The total effect of all these DOS changes on the surface electron distribution can be seen in our calculated total electron density (Fig. 11). The SR's described above are clearly visible as increases in electron density, compared to the bulk, above both surface-bilayer Ti and C atoms.

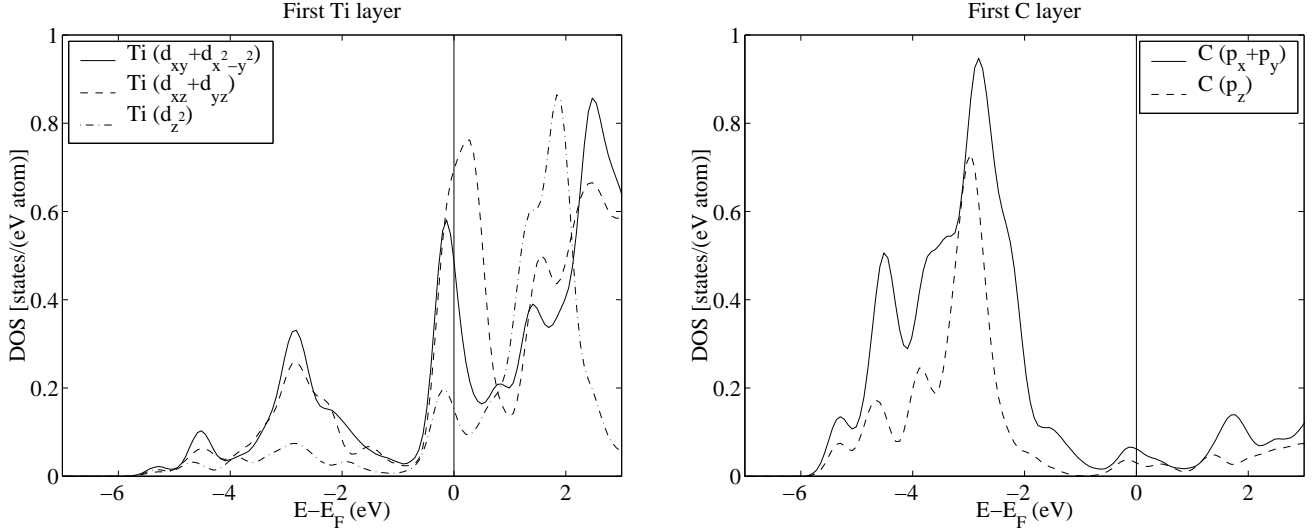


FIG. 7: Atom- and orbital-projected LDOS( $E$ )'s for the top TiC bilayer of the clean TiC(111) surface.

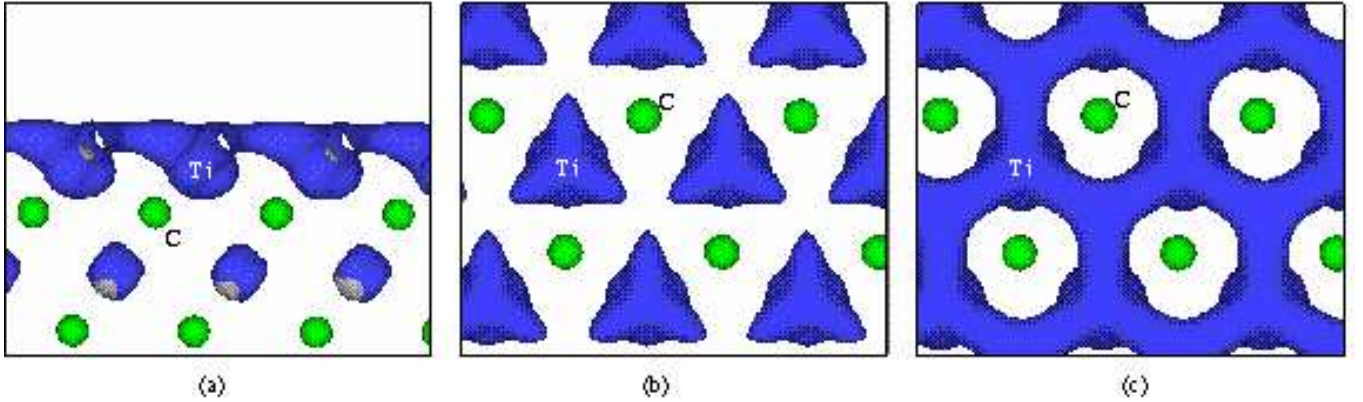


FIG. 8: (Color online). Three-dimensional real-space contour plots of DOS( $\mathbf{r}, E$ ), summed over all occupied electronic states above  $-0.6$  eV, for the clean TiC(111) surface, showing the Fermi-level surface resonance (TiSR). The plot is viewed (a) perpendicularly to the surface and (b–c) from above the surface (showing only the top TiC bilayer). Plot (b) shows a higher DOS value than plot (c). Green balls are C atoms. The Ti atoms lie inside the electron clouds, as marked in the figures.

### 3. Electronic Structure: TiC(001)

For comparison, we have also calculated the DOS( $E$ ) for the relaxed TiC(001) surface (Fig. 12). No clear SR is present at  $E_F$  on this surface. The surface-layer DOS( $E$ ) is very similar to the bulk DOS( $E$ ), apart from a shift of the main LVB and UVB peaks by 0.8 eV toward  $E_F$ . In particular, the lower part of the UVB is still characterized by only one peak, like the bulk UVB.

Like on TiC(111), however, changes occur in the high-energy part of the bulk UVB. As discussed above, this part is characterized by the ionic-covalent Ti–C bonds. Like for TiC(111), the creation of the (001) surface breaks these bonds and can therefore be expected to modify the electronic structure at these energies. In particular, like on TiC(111), the strong high-energy peak of the bulk UVB is quenched. Also, orbital analysis shows en-

ergetical shifts of the  $Ti d_{z^2}$  states lying in this region. These are, in a similar way as for TiC(111), indications of electron-structure changes due to the breakage of the bulk Ti–C bonds that cross the (001) cleavage plane.

Thus, compared to the (111) surface, the nonpolar TiC(001) surface shows no clear sign of CSR's in the lower part of the UVB nor of a TiSR around  $E_F$ . On the other hand, SR's appear in the upper part of the UVB, due to the breakage of Ti–C bonds.

### C. Atomic adsorption on TiC(111) and TiC(001)

To understand the nature of chemisorption on TiC(111), we perform a trend study, in which adsorption of the first-period element H, of the second-period elements B, C, N, O, F, and of the third-period elements

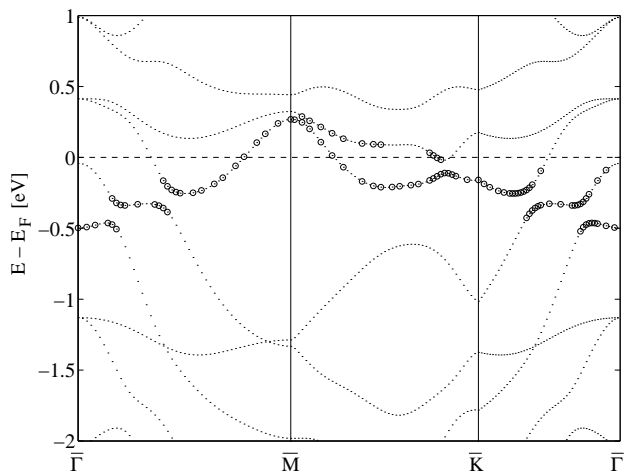


FIG. 9: Part of the calculated band structure around  $E_F$  for a TiC(111) slab with four TiC bilayers. Real-space plots of  $|\Psi_{n\mathbf{k}}(\mathbf{r})|^2$  for a number of the states belonging to the bands closest to  $E_F$  have been inspected. Those states that show a strong surface localization in these plots are marked in the figure with circles. The high-symmetry points in the two-dimensional Brillouin zone are  $\bar{\Gamma} = (0, 0)$ ,  $\bar{M} = (\frac{1}{2}, 0)$ , and  $\bar{K} = (\frac{1}{3}, \frac{1}{3})$ , where the coordinates are given relative to the surface reciprocal unit cell.

Al, Si, P, S, Cl are considered. For comparison, the adsorption of O on TiC(001) is also considered.

For TiC(111), all possible adsorption sites are considered: the two different three-foldly coordinated hollow sites, the two-foldly coordinated bridge site, and the top site. The two hollow sites differ by their relation to the structure of the second atomic layer of the substrate: the site is either located directly above a second-layer C atom or it is not, corresponding to the hcp and the fcc sites, respectively. The only information present in the literature regarding the adsorption geometry on TiC(111) concerns oxygen, which has been found to adsorb dissociatively in the fcc site,<sup>25</sup> and hydrogen, which has been found to adsorb in a three-fold hollow site, presumably the fcc site.<sup>26</sup>

For TiC(001), two different sites are considered: on top of a C atom and on top of a Ti atom. Previous studies have shown that oxygen adsorbs dissociatively on TiC(001), and that the preferred adsorption site is on top of the C atom.<sup>61,62,63,64</sup>

The structure of this subsection is as follows. First (Sec. III.C.1), the calculated energetics and relaxed geometries of all adsorbate systems are presented. Then (Sec. III.C.2), the calculated electronic structures of the systems with adatoms adsorbed in the stable fcc site of TiC(111) are described and analyzed in detail. For comparison, the electronic structures of the O adatom adsorbed in the hcp and top sites on TiC(111) and in the stable on-top-C site on TiC(001) are also calculated and analyzed. Finally (Sec. III.C.3), a model for the adsorption mechanism on TiC(111) is proposed, on the basis of these results.

### 1. Energetics and geometry

For each adatom, total-relaxation calculations are performed, yielding the ground-state equilibrium geometry and adsorption energy  $E_{\text{ads}}$ , corresponding to the energy gained by the formation of adatom-substrate bonds (see Sec. II). A higher value of  $E_{\text{ads}}$  implies a stronger adatom-substrate bond. Thus, analyses of the  $E_{\text{ads}}$  values give information about the preferred adsorption site for an adatom and a relative measure of the bond strengths of different adatoms on a surface.

The calculated  $E_{\text{ads}}$  values for the adatoms in the different sites on TiC(111) are listed in Table I. For the fcc, hcp, and top sites, the values given are those obtained after full relaxation of the adsorbate and substrate atoms in all directions, with the exception of B, C, and N adatoms in top site, for which small forces ( $\sim 0.05$  eV/Å) toward the neighboring fcc sites are still present after relaxation. No adatom binds in the bridge site, all of them relaxing to the neighboring fcc site. Thus, the  $E_{\text{ads}}$  values given for the bridge site are those obtained after full relaxation of the adatoms in only the direction perpendicular to the substrate and of the substrate atoms in all directions.

All adatoms prefer to adsorb in the fcc site, followed by the metastable hcp site, where the adsorption energy in most cases is very close to that of the unstable bridge site. The bond to the top site is significantly weaker than to the other sites and the top-site potential-energy surface (PES) has a rather shallow energy minimum, a small deviation from the optimum relaxed position being sufficient for destabilization and relaxation toward a neighboring fcc site. The overall energetical preference for the fcc site agrees with the experimental results for oxygen and hydrogen adsorption on TiC(111).<sup>25,26</sup>

The strongest fcc bond is obtained for oxygen, almost 9 eV/atom, followed by C, N, S, and F, the energies for C and N being almost the same. The weakest bonds are obtained for Al and H. The variation in  $E_{\text{ads}}$  values is very large, from 3.4 eV/atom for Al to 8.8 eV/atom for O.

Also, the energy differences  $\Delta E_{\text{ads}}$  between the different adsorption sites (Table I) vary very strongly between the adatoms. In particular, the bridge site can be used as an approximation for the transition state between the fcc and hcp sites. The energy barriers for diffusion between fcc and hcp sites can then be estimated from the differences between the  $E_{\text{ads}}$  values calculated for the fcc/hcp sites and the bridge site. The estimated barriers for diffusion from fcc to hcp site thus calculated vary from 0.12 eV for Al to 1.14 eV for C. The smallest barriers are obtained for Al, Cl, Si, H, F, and S, in order of increasing barrier height.

In addition, it is interesting to study the  $E_{\text{ads}}$  differences between fcc and hcp sites. The smallest such differences are obtained for Al, B, and Si, in order of increasing difference. On the other hand, the strongest preference for fcc site is obtained for N, O, and C.

Thus, of all considered adatoms, Al and Si appear to

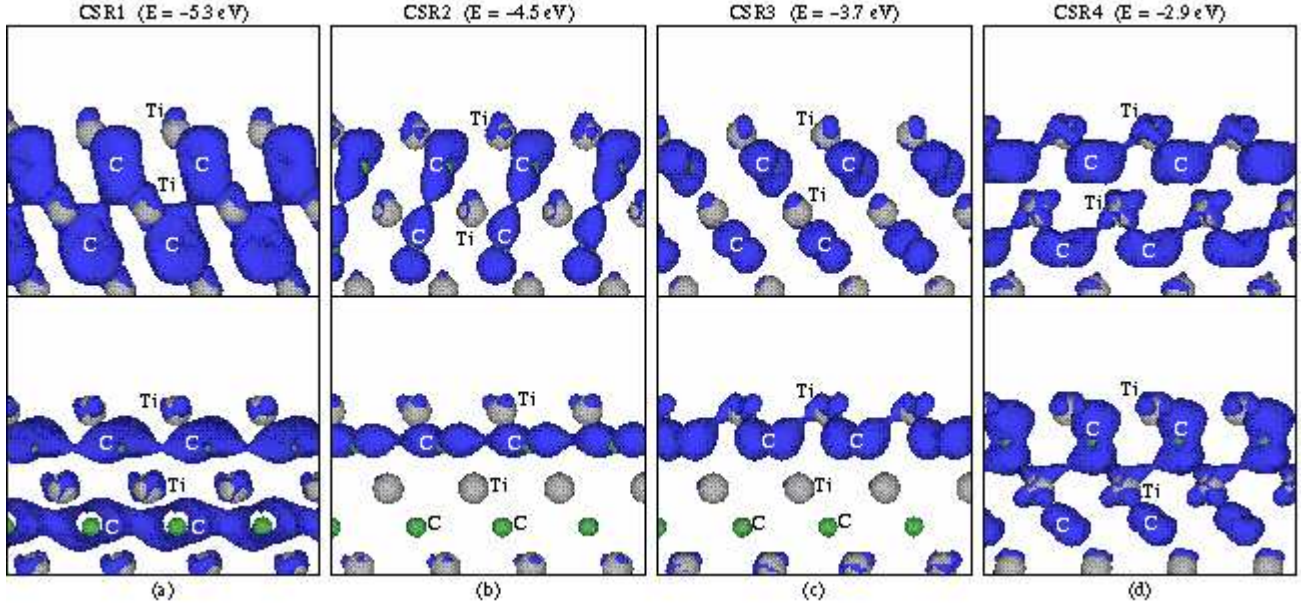


FIG. 10: (Color online). Three-dimensional real-space contour plots of  $\text{DOS}(\mathbf{r}, E)$  for the clean TiC(111) surface, at selected energies  $E$  close to the energies of the four UVB peaks CSR1–CSR4 of the surfaces  $\text{DOS}(E)$  (Fig. 6). For each UVB peak [(a)–(d)], two different electronic states, lying very closely in energy, are shown in order to illustrate the mixed  $p_{xy} + p_z$  symmetry of each peak. The plots are viewed perpendicularly to the surface. C (Ti) atoms are green/darker (grey/lighter) balls, or lie inside the electron clouds, as marked in the figures. For different (same) CSR’s, the plots correspond to different (same) values of  $\text{DOS}(\mathbf{r}, E)$ .

TABLE I: Calculated atomic adsorption energies  $E_{\text{ads}}$  for the different adsorption sites on the TiC(111) surface. For all adatoms, the bridge site is unstable and relaxes to the neighboring fcc site. The values correspond to full relaxation of the adatom and surface-bilayer atomic coordinates, except for the bridge-site values, for which the adatom has only been relaxed in the direction perpendicular to the surface. Also given are the energy differences  $\Delta E_{\text{ads}}$  between the fcc/hcp and the bridge sites and between the fcc and the hcp sites.

atom	$E_{\text{ads}}$ (eV/atom)				$\Delta E_{\text{ads}}$ (eV/atom)		
	fcc site	hcp site	top site	bridge site	fcc–bridge	hcp–bridge	fcc–hcp
H	3.60	3.34	2.31	3.27	0.33	0.07	0.26
B	5.68	5.55	3.68	4.92	0.76	0.63	0.13
C	7.87	7.15	4.69	6.73	1.14	0.42	0.72
N	7.86	6.87	4.59	6.77	1.09	0.10	0.99
O	8.75	7.93	6.50	7.95	0.80	−0.02	0.82
F	6.92	6.46	6.01	6.58	0.34	−0.12	0.46
Al	3.36	3.31	2.78	3.24	0.12	0.07	0.05
Si	5.06	4.89	3.95	4.74	0.32	0.15	0.17
P	5.87	5.61	4.49	5.00	0.87	0.61	0.26
S	7.09	6.78	5.68	6.75	0.34	0.03	0.31
Cl	5.48	5.20	4.51	5.25	0.23	−0.05	0.28

possess the most planar PES’s between the fcc and hcp sites, having *both* small estimated diffusion barriers *and* very similar  $E_{\text{ads}}$  values for the fcc and hcp sites. This indicates that the directionality of the adatom–substrate bond is weak for these two adatoms. This is very interesting, considering the possibility that the high plasticity of MAX phases such as  $\text{Ti}_3\text{SiC}_2$  and  $\text{Ti}_3\text{AlC}_2$  could be caused by a good lateral mobility between the layers of

Si/Al atoms and  $\text{Ti}_6\text{C}$  octahedra that make up their bulk structures.<sup>13</sup>

On the other hand, the C and N adatoms show a strong directionality of bonds to the substrate, having both high diffusion barriers and a high preference for the fcc site, with the C adatom having highest barriers. This is consistent with the strong hardness and resistance against deformation of bulk TiC and TiN, TiC being the hardest



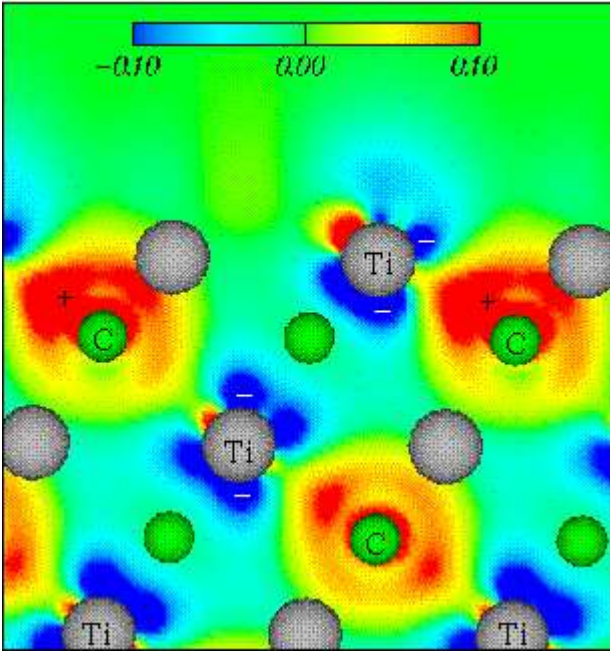


FIG. 11: (Color online). Contour plot (through a plane containing the Ti and C atoms marked in the figure) of the difference between the total electron density at the TiC(111) surface and the free-atomic densities. Green/darker (grey/lighter) balls are C (Ti) atoms. Only the atoms lying in the drawn contour-plot plane are marked by names, the remaining atoms lying in front of the plane. Red/dark (blue/black) regions correspond to positive (negative) electron-density differences, as exemplified in the figure by the + and - signs.

TABLE II: Calculated, fully relaxed, atomic adsorption energies  $E_{\text{ads}}$  for O in top-C and top-Ti sites on the TiC(001) surface.

	$E_{\text{ads}}$ (eV/atom)	
	top-C site	top-Ti site
O/TiC(001)	4.96	2.95

one, described in the literature.<sup>54</sup>

For O on TiC(001) (Table II), our results confirm the preference for adsorption in the on-top C site that has been reported in the literature.<sup>61,62,63,64</sup> Also, our calculated energy difference between on-top C and on-top Ti site (2.01 eV/atom) compares well with the value from cluster DFT calculations (2.25 eV/atom).<sup>63</sup>

For the TiC(111) fcc site, the adsorption energies for second- and third-period elements show similar trends (Fig. 13), the only difference being the very similar values for C and N. In both periods, the binding is strongest for the group-VI elements (O and S) and decreases monotonically (again, with the exception of C and N) when moving away from group VI. Also, it decreases from second- to third-period elements. For O in the preferred site (on-top C) on TiC(001), the adsorption is 43% weaker than

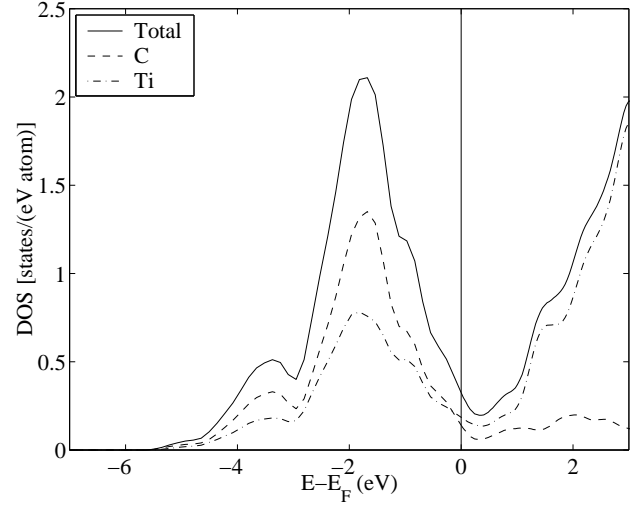


FIG. 12: Total and atom-projected DOS( $E$ ) for the top atomic layer of the clean TiC(001) surface.

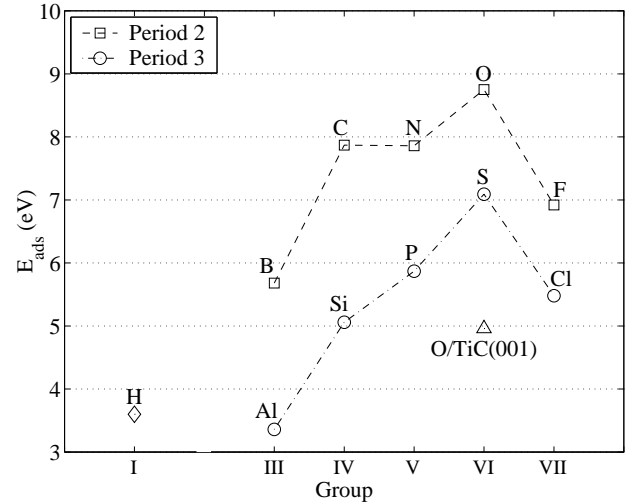


FIG. 13: Calculated, fully relaxed, atomic adsorption energies  $E_{\text{ads}}$  for the fcc site on the TiC(111) surface, showing the adsorption-strength trends. Also shown is the adsorption energy for O in the most stable TiC(001) site (on-top C).

on TiC(111) (Fig. 13).

The calculated relaxed atomic distances between the adsorbates in the fcc site and their nearest neighbors on the TiC(111) substrate (Table III) show similar trends within the two adatom periods: both the adsorbate-substrate distances and the substrate Ti-Ti distances are smallest for group-V and/or group-VI elements and increase monotonically when moving away from them. This is again an indication of the particularly strong chemisorption of group-V and VI elements. For most adatoms, the Ti-Ti distances are smaller than the clean-surface values, indicating a strong adatom-Ti attraction. Overall, the adatom-substrate distances are larger for period 3, due to the extra filled electron shell in the third-

TABLE III: Calculated geometries of the relaxed adsorbate-TiC(111) systems for all considered adatoms in fcc site:  $d_{\text{ad-Ti}}$  and  $d_{\text{ad-C}}$  are the distances between the adatoms and their nearest-neighbor Ti and C atoms, respectively;  $Z_{\text{ad-TiC}}$  is the perpendicular distance between the adatoms and the TiC(111) surface;  $d_{\text{Ti-Ti}}$  and  $d_{\text{C-C}}$  are the Ti-Ti and C-C distances within the surface TiC(111) bilayer, close to the adatom; and  $d_{\text{Ti-C}}$  is the distance between the Ti and C atoms closest to the adatom. The bond distances in the first TiC bilayer on the clean TiC(111) surface are included for comparison. All values are in Å.

atom	$d_{\text{ad-Ti}}$	$d_{\text{ad-C}}$	$Z_{\text{ad-TiC}}$	$d_{\text{Ti-Ti}}$	$d_{\text{C-C}}$	$d_{\text{Ti-C}}$
H	2.01	2.73	1.03	2.98	3.08	2.04
B	2.16	3.01	1.32	2.95	3.08	2.06
C	1.99	2.86	1.10	2.88	3.09	2.07
N	1.94	2.80	1.02	2.85	3.08	2.06
O	1.98	2.81	1.07	2.88	3.08	2.05
F	2.16	2.93	1.28	3.00	3.07	2.04
Al	2.67	3.54	2.02	3.03	3.07	2.05
Si	2.52	3.39	1.82	3.00	3.07	2.05
P	2.44	3.32	1.72	2.99	3.07	2.06
S	2.44	3.30	1.72	3.00	3.07	2.05
Cl	2.54	3.35	1.82	3.06	3.07	2.04
Clean surface	—	—	—	3.06	3.06	2.04

period adatoms.

## 2. Electronic Structure

In order to understand the nature of the chemisorption bond and trends, we analyze the electronic structure of all the considered adsorbates in the fcc site on TiC(111), of the O adatom in hcp and top site on TiC(111), and of the O adatom in the on-top-C site on TiC(001).

For each considered system, two different types of DOS's are calculated (see also Sec. II): (i) the difference in total, atom-, and orbital-projected DOS( $E$ ) between the relaxed adsorbate+slab system and the corresponding slab with no adsorbate but with Ti and C atoms in the same positions [ $\Delta\text{DOS}(E)$ ]; (ii) the distribution in real space of the contribution to the total DOS from specific energy values [ $\text{DOS}(\mathbf{r}, E)$ ]. Also, the distribution of the total electron density around the studied adatoms, compared to the free-atom density, is shown. A measure of the localization of charge around each atom is obtained with the Bader method (Sec. II).

The  $\Delta\text{DOS}(E)$  plots (also called adsorbate-induced DOS's)<sup>65</sup> show how the adsorption modifies the electronic structure in the surface region, for instance, by the appearance of chemical bonds between the adsorbate and the substrate. A negative  $\Delta\text{DOS}$  peak at a specific energy  $E_0$  corresponds to a quenching of the electronic states having energy  $E_0$ , while a positive  $\Delta\text{DOS}$  peak at  $E_1$  corresponds to the appearance of new states at

$E_1$ . Thus, for instance, a negative peak at energy  $E_0$ , surrounded by two positive peaks at energies  $E_1 < E_0$  and  $E_2 > E_0$ , can be interpreted as evidence for the hybridization of the states at  $E_0$  with adatom states, resulting in the formation of bonding and antibonding states at  $E_1$  and  $E_2$ , respectively.

Projections of the  $\Delta\text{DOS}(E)$  onto individual atoms and atomic orbitals in the surface-bilayer region give more detailed information on the nature of these bonds. Such information is complemented by visualizations in three-dimensional real space of the DOS( $\mathbf{r}, E$ ) for all electronic states within the TiC(111) UVB and TiSR regions, thus providing vivid state-resolved illustrations of the bonds. Finally, the Bader and total charge-density analyses give information on the amount of charge transfer from substrate to adatom and on the charge polarization around each adatom, thus providing indications on the degree of covalency *vs.* ionicity of the adatom-substrate bonds.

Starting with the H adatom, which demonstrates all the key features, this subsection describes all our electron-structure results for the studied adatoms in deep detail and compares them with available experimental information. In the following subsection (Sec. III.C.3), this information is analyzed and used as basis for the formulation of a model describing the adsorbate-substrate interaction.

(a) *H adatom in fcc site on TiC(111)*. The calculated  $\Delta\text{DOS}(E)$  for an H adatom adsorbed in the fcc site on TiC(111) (Fig. 14) is characterized by (i) two strong negative peaks around  $E_F$ , of almost exclusively Ti character (one peak, of mainly  $d_{(xy,x^2-y^2)}$  symmetry, lies at  $-0.2$  eV, and the other one, of almost exclusively  $d_{(xz,yz)}$  symmetry, lies at  $+0.4$  eV); (ii) a strong positive peak at  $+1.1$  eV, of almost exclusively Ti  $d$  character (with mixed  $d$  symmetry); (iii) a strong negative peak at  $-3.9$  eV, of mainly C character; (iv) a broad positive region between  $-6.1$  and  $-4.1$  eV (with two main peaks at  $-5.5$  and  $-5.0$  eV and a smaller one at  $-4.3$  eV), composed mainly of H  $s$  states, with minor contributions from the substrate C and Ti atoms for the two main peaks; and (v) a positive region between  $-3.6$  and  $-0.7$  eV (with peaks at  $-3.1$ ,  $-2.3$ , and  $-1.4$  eV), composed mainly of C-centered states.

The three-dimensional, real-space, plots of DOS( $\mathbf{r}, E$ ) show that (i) the peaks at  $-5.5$  and  $-5.0$  eV correspond mainly to strong H-C bonding states [Fig. 15(a)], with weaker contributions from H-Ti bonding states; (ii) weaker H-Ti and H-C bonding states are present around the peak at  $-4.3$  eV; (iii) bonding H-Ti states are present around the peaks at  $-3.1$  [Fig. 15(b)] and  $-2.3$  eV. In addition, the DOS( $\mathbf{r}, E$ ) summed over all occupied states above  $-0.3$  eV [Fig. 15(c)] clearly shows the depletion of TiSR around the adsorbed H atom.

Our prediction of strong H  $s$ -derived peaks at  $-5.5$  and  $-5.0$  eV can be compared with the experimental finding of an H  $1s$  state between approximately  $-5.5$  and  $-6.5$  eV for full ( $1 \times 1$ ) monolayer coverage of H on TiC(111).<sup>27</sup>



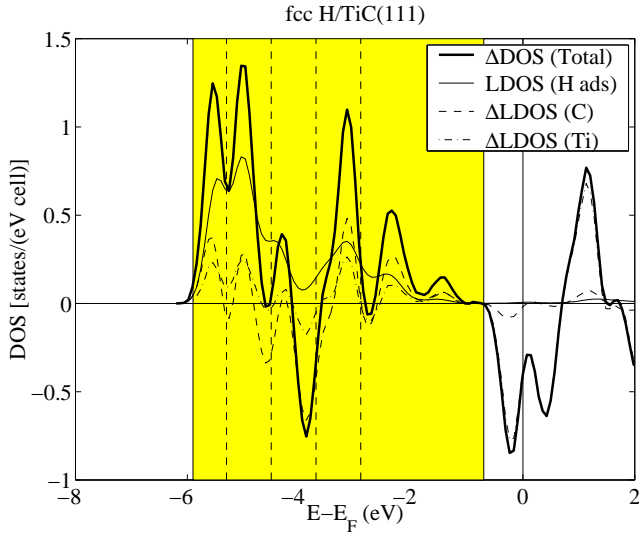


FIG. 14: Calculated density of states (DOS) for an H atom adsorbed in the fcc site on the TiC(111) surface. The thin line shows the DOS projected on the H adatom. The other three lines show the difference in DOS (“ $\Delta$ DOS”) between the relaxed slab *with* adsorbed fcc H and a slab *without* H adatom but with Ti and C coordinates fixed to the same values as those of the relaxed slab+adsorbate system. The dashed (dot-dashed) line shows the  $\Delta$ DOS projected on all the C (Ti) atoms of the first TiC bilayer of the TiC(111) surface. The thick line shows the total  $\Delta$ DOS for the adsorbate+first-TiC-bilayer system. The shaded area shows the energetical location of the UVB of the clean TiC(111) surface. The dashed vertical lines mark the energetical locations of the four UVB peaks of clean TiC(111).

Also, our prediction of a sharp DOS decrease around  $E_F$  compares well with published experimental results.<sup>21</sup>

The total electron density around the H adatom (Fig. 16) shows an excess of electrons (compared to a free H atom) around the adatom. Our Bader analysis of the charge localization yields an “ionicity” (*i.e.*, charge difference compared to the neutral atom) of  $-0.64|e|$  (where  $|e|$  is the electronic charge) around the H adatom and a decrease of charge, compared to the clean TiC(111) surface, around its nearest-neighbor (NN) Ti and C atoms (Table IV). Thus, electrons have transferred from both the Ti and C atoms in the surface bilayer to the adatom. The extra electrons around the adatom show an almost spherical distribution, typical of the  $s$  orbital, although a polarization toward the NN Ti atom can be seen.

(*b*) *Second-period adatoms (B, C, N, O, and F) in fcc site on TiC(111)*. The calculated  $\Delta$ DOS( $E$ ) and total electron densities for the second-period adatoms adsorbed in the fcc site on TiC(111) are shown in Figs. 17 and 18. Also, the calculated ionicities (*i.e.*, charge differences compared to the neutral atoms) for the adatoms and their Ti and C NN’s, obtained from Bader analyses, are given in Table IV.

**B adatom:** For B, the  $\Delta$ DOS( $E$ ) (Fig. 17) is characterized by (i) a strong negative double-peak structure

TABLE IV: Charge localization around all the considered adatoms and their nearest-neighbor (NN) Ti and C atoms, as calculated from our Bader analyses. The values given in the table are the “ionicities” of the different atoms, that is, the atomic charge values compared to the neutral atoms, given in units of electron charge  $|e|$ . For comparison, the corresponding values for the Ti and C atoms of the surface bilayer of the clean TiC(111) surface are also given.

adatom	ionicity		
	adatom	NN Ti	NN C
H	-0.64	+1.24	-1.75
B	-1.09	+1.20	-1.65
C	-1.35	+1.32	-1.65
N	-1.35	+1.36	-1.68
O	-1.17	+1.34	-1.68
F	-0.80	+1.28	-1.72
Al	-0.47	+1.08	-1.71
Si	-0.93	+1.19	-1.69
P	-1.12	+1.25	-1.68
S	-1.06	+1.29	-1.70
Cl	-0.75	+1.26	-1.73
Clean surface	—	+1.09	-1.79

at  $-0.2$  and  $+0.3$  eV, of almost exclusively Ti character (with mainly mixed  $d_{(xy,x^2-y^2)}$  and  $d_{(xz,yz)}$  symmetry for the peak at  $-0.2$  eV, and almost exclusively  $d_{(xz,yz)}$  symmetry for the peak at  $+0.3$  eV); (ii) a positive peak, of mainly  $Tid_{(xz,yz)}$  character, at  $+1.0$  eV; (iii) much smaller negative peaks, of mainly C character, at  $-4.7$ ,  $-3.9$ , and  $-2.9$  eV; (iv) a main positive peak at  $-0.7$  eV, mainly composed of Ti and B  $p$  states; (v) a smaller positive peak at  $-5.8$  eV, of mainly B  $s$  character; (vi) much smaller positive peaks at  $-5.1$  eV (of mainly B  $s$  character) and at  $-3.2$  eV (of mainly C and B  $s$  character); (vii) a positive region between  $-2.7$  eV and the main positive peak, including a peak at  $-2.4$  eV, of mainly C character.

The DOS( $\mathbf{r}, E$ ) plots show that (i) the peak at  $-0.7$  eV consists of very strong B–Ti bonding states; (ii) the peak at  $-5.8$  eV consists of very strong B–C bonding states and of weaker B–Ti bonding states; (iii) the peak at  $-5.1$  eV consists of weak B–Ti and B–C bonding states; (iv) only B–Ti bonding states are detected around  $-3.2$  eV; (v) the only type of bonding states detected between  $-2.7$  eV and the main positive peak are weak B–Ti states; (vi) similarly to the case of H [Fig. 15(c)], the large negative peak just below  $E_F$  corresponds to a strong depletion of the TiSR around the B adatom.

The total electron-density plot [Fig. 18(a)], together with the calculated Bader charges (Table IV), show, similarly to the H adatom, a significant charge transfer from the surface-bilayer Ti and C atoms to the B adatom, yielding a B adatom ionicity of  $-1.09|e|$ . In contrast to the H adatom, however, the distribution of the excess electrons around the B adatom shows a  $p_{xy}$ -like symme-

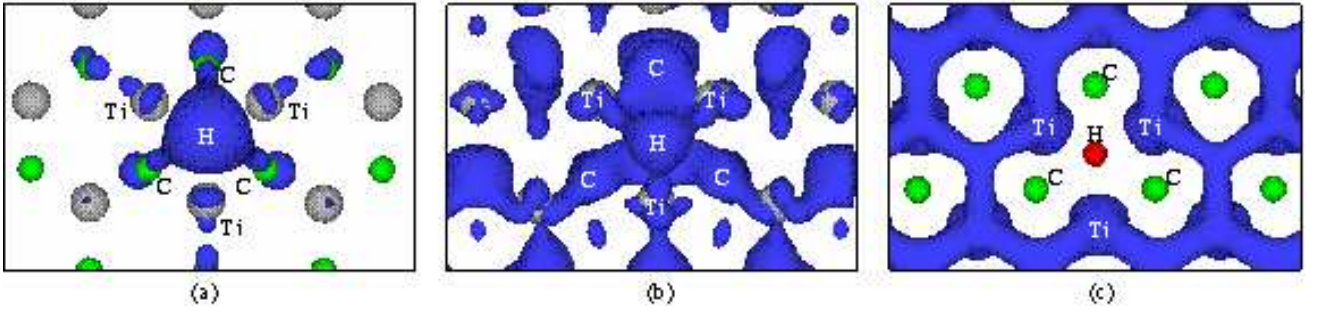


FIG. 15: (Color online). Three-dimensional contour plots of the calculated  $\text{DOS}(\mathbf{r}, E)$ , at different energies  $E$ , for an H atom adsorbed in the fcc site on the TiC(111) surface. All three plots are viewed from above the surface, showing only the adatom and the top TiC bilayer, and correspond to (a)  $E = -5.5$  eV, showing the strong H-C bonding character of the lowest  $\Delta\text{DOS}$  peak (Fig. 14); (b)  $E = -3.1$  eV, showing the H-Ti bonding character of the  $\Delta\text{DOS}$  peak at  $-3.1$  eV; and (c) the sum of all occupied states above  $E = -0.3$  eV, showing the strong depletion of TiSR in the region around the H adatom. As marked in each plot, the smaller (green/darker) balls are C atoms, the larger (grey/lighter) balls are Ti atoms, and the red/darkest ball is the H adatom [in (a)–(b), the H adatom lies inside the electron cloud]. In (b), the electron cloud around the H atom connects only to the neighboring Ti atoms, while the C-centered electron clouds connect only to the neighboring C and Ti atoms and lie below the H-Ti bonding clouds.

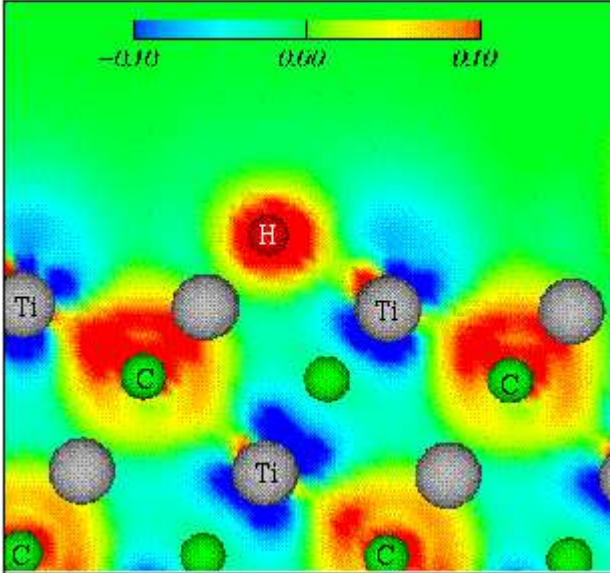


FIG. 16: (Color online). Same as Fig. 11 but for the system with an H adatom adsorbed in fcc site on the TiC(111) surface. The (darkest) red ball is the adatom.

try, extending clearly toward the NN Ti atoms. Also, an electron depletion can be observed directly above the B adatom, again indicating a strong polarization of the adatom electronic distribution toward the substrate.

**C adatom:** For C, the  $\Delta\text{DOS}(E)$  (Fig. 17) shows (i) again a large negative double-peak structure at  $-0.2$  and  $+0.3$  eV, of predominantly Ti character (with mixed  $d_{(xy, x^2-y^2)}$  and  $d_{(xz, yz)}$  symmetry for the peak at  $-0.2$  eV, and only  $d_{(xz, yz)}$  symmetry for the peak at  $+0.3$  eV), similar to the one for B but with a slightly wider low-energy peak; (ii) a positive peak, of predominantly  $\text{Ti}d_{(xz, yz)}$  character, at  $+1.0$  eV; (iii) a main positive

peak, of mainly adatom-C  $p$  and Ti character, at  $-1.3$  eV; (iv) a smaller positive peak, of mixed adatom and substrate character, at  $-3.1$  eV.

The  $\text{DOS}(\mathbf{r}, E)$  plots show that (i) the main positive peak corresponds to very strong adatom-C-substrate-Ti bonding states; (ii) the smaller positive peak is composed of weak adatom-C-substrate-Ti and adatom-C-substrate-C bonding states; (iii) the large negative peak just below  $E_F$  is characterized by a depletion of the TiSR around the C adatom.

The total electron-density plot [Fig. 18(b)] and Bader charges (Table IV) are similar to those for the B adatom, with a significant electron transfer from the surface-bilayer Ti and C atoms to the C adatom, these electrons assuming a clear  $p_{xy}$ -like symmetry around the adatom and extending toward the NN Ti atoms. Also, an electron depletion is again found directly above the adatom, indicating a strong electronic polarization toward the substrate. Compared to the B adatom, however, the electron transfer is larger, the calculated C adatom ionicity being  $-1.35|e|$ . Also, the polarization toward the NN Ti atoms is slightly smaller.

**N adatom:** For N, the  $\Delta\text{DOS}(E)$  (Fig. 17) displays (i) again a negative double-peak structure, of Ti character, at  $-0.3$  and  $+0.3$  eV, with the same orbital symmetries as for B and C, but with the low-energy peak slightly weaker than that for B and C; (ii) a positive peak, of mainly  $\text{Ti}d_{(xz, yz)}$  character, at  $+1.3$  eV; (iii) in contrast to the other period-two adatoms, a broad positive region that extends between  $-5.9$  and  $-0.9$  eV, composed of five peaks (a main peak, at  $-3.4$  eV, which shows mainly N  $p$  and Ti character, two minor peaks at  $-5.4$  and  $-4.7$  eV, which show mainly C character, and two intermediate peaks, at  $-3.9$  and  $-2.4$  eV, which show mainly N  $p$  character).

The  $\text{DOS}(\mathbf{r}, E)$  plots show that (i) the states below  $\sim -3.7$  eV consist of mainly N-C bonding states, to-

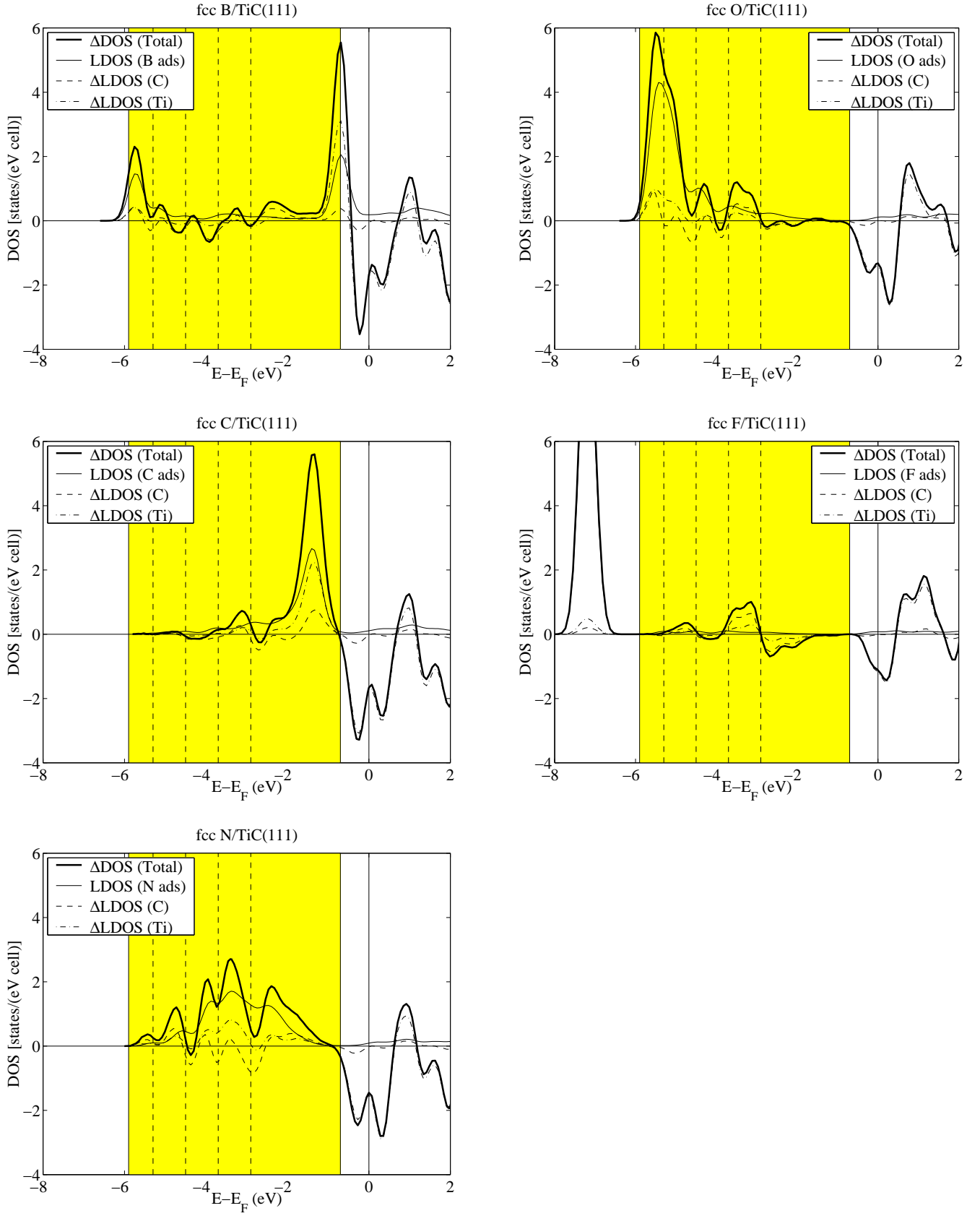


FIG. 17: Same as Fig. 14 but for the second-period elements B, C, N, O, and F.



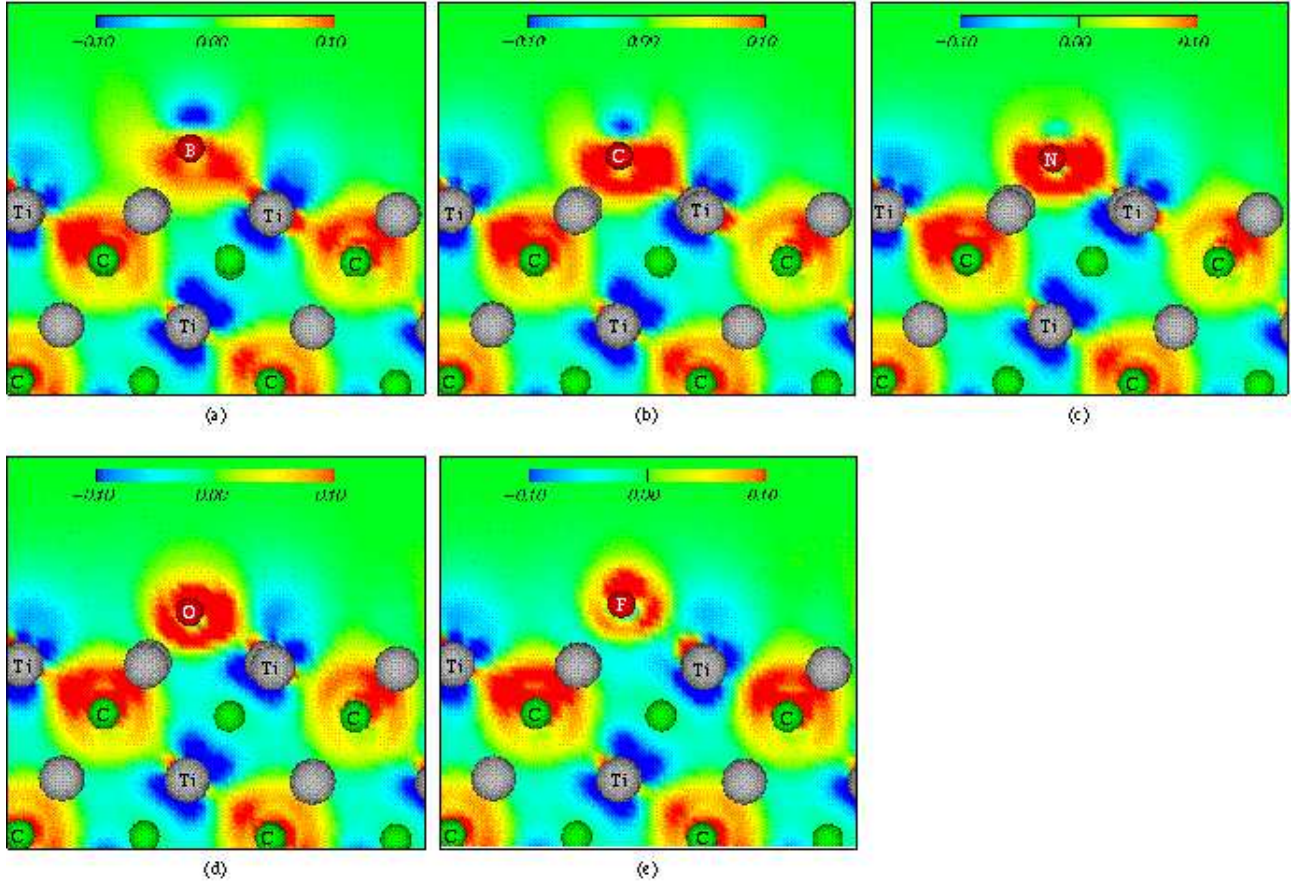


FIG. 18: (Color online). Same as Fig. 16 but for the systems with the second-period adatoms (a) B, (b) C, (c) N, (d) O, and (e) F adsorbed in fcc site on the TiC(111) surface.

gether with weaker N–Ti bonding states; (ii) the region around  $-3.4$  eV consists of approximately equally strong N–C and N–Ti bonding states; (ii) the region above  $-2.9$  eV consists exclusively of N–Ti bonding states; (iii) the region of the negative peak just below  $E_F$  is characterized by a depletion of the TiSR around the N adatom and by the presence of a very small N-centered dangling bond.

The total electron-density plot for N [Fig. 18(c)] is very similar to that for C. However, the adatom electrons assume a slightly more spherically symmetric distribution, that is, the polarization toward the substrate, and in particular toward the NN Ti atoms, although still present, is smaller than in the case of the C adatom. The total electron transfer from the surface-bilayer Ti and C atoms to the N adatom is identical to that for the C adatom, yielding the same adatom ionicity ( $-1.35|e|$ ).

**O adatom:** For O, the  $\Delta\text{DOS}(E)$  (Fig. 17) shows (i) a negative, Ti-dominated, double-peak structure at  $-0.2$  and  $+0.3$  eV, with the same orbital symmetries as B, C, and N, but with the low-energy peak weaker than for B, C, and N; (ii) a positive double-peak structure, of Ti character, above  $E_F$  (one peak, at  $+0.8$  eV, shows mainly  $d_{(xz,yz)}$  symmetry, while the other peak, at  $+1.6$

eV, shows almost exclusively  $d_{z^2}$  symmetry); (iii) a main positive peak, of mainly O  $p$  character, at  $-5.5$  eV; (iv) smaller positive peaks at  $-4.3$  (of almost exclusively O  $p$  character) and at  $-3.5$  eV (of mainly C and  $Op_z$  character).

The main positive peak, at  $-5.5$  eV, is slightly broadened, with a shoulder on its high-energy side. While the main peak displays equally large Ti and C character, the higher-energy shoulder shows almost no C character. A projection of the peak onto O  $p_{xy}$  and  $p_z$  orbitals reveals that these are displaced from one another: the O  $p_{xy}$  peak lies at  $-5.4$  eV, while the O  $p_z$  peak lies at  $-5.1$  eV. The main part of the peak is thus composed of O  $p_{xy}$  orbitals, while the shoulder at higher energy is caused by the O  $p_z$  orbitals.

This prediction of strong O  $p$  states around  $-5.5$  eV agrees well with the experimental finding of O  $2p$  states between approximately  $-5.0$  and  $-6.5$  eV for full ( $1 \times 1$ ) monolayer coverage of O on TiC(111).<sup>28</sup> Also, the same experimental study indicates that the O  $2p_z$  state has a higher energy than the O  $2p_{xy}$  states, in good agreement with our results. In addition, our predicted sharp decrease in DOS around  $E_F$  agrees also very well with published experimental results.<sup>19</sup>

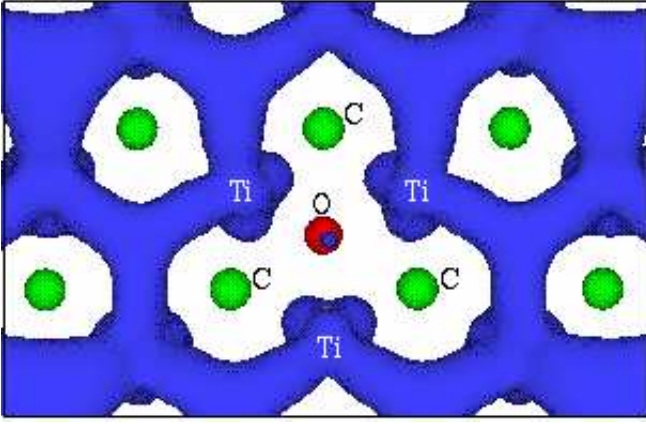


FIG. 19: (Color online). Same as Fig. 15(c) but for an O adatom adsorbed in fcc site on TiC(111). A small DOS above the O adatom, of clear dangling-bond character, can be seen.

The DOS( $\mathbf{r}$ ,  $E$ ) plots for adsorbed O show that (i) the main, broadened, positive peak consists of very strong O–Ti and O–C bonding states; (ii) only O–Ti bonding states are present around the smaller positive peaks; (iii) the region of the negative peak just below  $E_F$  is characterized by a depletion of the TiSR around the O adatom and by a small O-centered dangling bond (see Fig. 19), slightly more pronounced than the one for N.

The total electron-density plot [Fig. 18(d)] shows a more symmetric distribution of the O adatom electrons than those of the previous second-period adatoms. Still, a polarization toward the NN Ti atoms can be seen. Again, the Bader charges (Table IV) show a significant electron transfer from the surface-bilayer Ti and C atoms, yielding an O adatom ionicity of  $-1.17|e|$ .

**F adatom:** For F, the  $\Delta\text{DOS}(E)$  (Fig. 17) shows (i) that the negative double peak around  $E_F$  is significantly smaller than for the previous period-two adatoms but still composed of a Ti  $d_{(xy,x^2-y^2)} + d_{(xz,yz)}$  peak at  $-0.1$  eV and of a Ti  $d_{(xz,yz)}$  peak at  $+0.3$  eV; (ii) a positive double-peak structure above  $E_F$ , at  $+0.7$  and  $+1.1$  eV, with mainly Ti  $d_{(xz,yz)}$  symmetry; (iii) a huge positive peak, of almost exclusively F  $p$  character, at  $-7.2$  eV; (iv) much smaller positive peaks, of mainly C character, at  $-4.8$ , at  $-3.5$ , and at  $-3.1$  eV; (v) small negative peaks, of C character, at  $-2.7$  and at  $-2.1$  eV.

The DOS( $\mathbf{r}$ ,  $E$ ) plots show that (i) the main peak consists of mainly F-centered states, with only slight bonding to the neighboring Ti and C atoms; (ii) no F–Ti or F–C bonding states are found around the smaller positive peaks; (iii) the negative-peak region just below  $E_F$  is again characterized by a depletion of the TiSR around the F adatom and by an F-centered dangling bond, stronger than for the previous second-period adatoms.

The total electron-density plot for F [Fig. 18(e)] is qualitatively different from those for the previous second-period adatoms. No polarization of the F adatom electron density toward the substrate is found, rather, there is a polarization toward the vacuum side of the adatom.

Still, some polarization toward the NN Ti atom can be detected, but this is much weaker than for the previous second-period adatoms, the electron-density difference being almost zero in-between the F–Ti bond. Again, the Bader charges (Table IV) show a significant electron transfer from the surface-bilayer Ti and C atoms to the F adatom, yielding an almost completely ionized F adatom, its ionicity being  $-0.80|e|$ .

(c) *Third-period adatoms (Al, Si, P, S, and Cl) in fcc site on TiC(111).* The calculated  $\Delta\text{DOS}(E)$  and total electron densities for the third-period adatoms adsorbed in the fcc site on TiC(111) (Figs. 20 and 21) show strong similarities to those calculated for the second-period elements.

**Al adatom:** For Al, the  $\Delta\text{DOS}(E)$  (Fig. 20) shows (i) a large negative double-peak structure at  $-0.1$  eV (of mainly  $\text{Ti}d_{(xy,x^2-y^2)} + d_{(xz,yz)}$  symmetry) and at  $+0.4$  eV (of exclusively  $\text{Ti}d_{(xz,yz)}$  symmetry); (ii) a positive double peak at  $+0.9$  and  $+1.6$  eV, both of predominantly Ti character, with mixed  $d$  symmetry; (iii) a main positive peak, of mainly Ti character, at  $-0.6$  eV; (iv) smaller negative peaks at  $-3.9$  eV, of mainly C character, and at  $-2.8$  eV, of C and Ti character; (v) small positive peaks, of mainly Al  $s$  character, at  $-5.5$ ,  $-4.9$ ,  $-4.3$ , and  $-3.2$  eV; (vi) a region of positive  $\Delta\text{DOS}$  between  $-2.7$  eV and the main positive peak, including a C-dominated peak at  $-2.4$  eV. Orbital projection of the Al states along the whole UVB region reveals that they display  $p$  symmetry above  $-1.2$  eV and  $s$  symmetry below  $-1.2$  eV.

The DOS( $\mathbf{r}$ ,  $E$ ) plots show that (i) the main peak consists of very strong Al–Ti bonding states; (ii) only Al–C bonding states are found in the region below  $-4.8$  eV; (iii) mainly Al–Ti bonding states (with weaker Al–C contributions) are found between  $-4.8$  and  $-4.2$  eV; (iv) only weak Al–Ti bonding states are present around the peak at  $-3.2$  eV; (v) almost no Al-centered states are found between  $-2.7$  eV and the main positive peak; (vi) the negative peak just below  $E_F$  is characterized by a depletion of the TiSR around the Al adatom.

The electron-density plots (Fig. 21) show clearly the overall larger radii of the third-period adatoms, compared to the second-period adatoms. Despite this, similarities are present. Similarly to B, the plot for Al [Fig. 21(a)] shows a strong polarization of the adatom charge toward the substrate and in particular toward the NN Ti atoms. Also, the Bader charges (Table IV) show again an electron transfer from the surface-bilayer Ti and C atoms to the Al adatom. However, this is significantly weaker than for the second-period adatoms, yielding an Al adatom ionicity of  $-0.47|e|$ .

**Si adatom:** For Si, the  $\Delta\text{DOS}(E)$  (Fig. 20) shows (i) a large, Ti-dominated, negative double-peak structure at  $-0.2$  and  $+0.4$  eV, with same orbital symmetries as for Al but with a slightly wider low-energy peak; (ii) a positive, Ti-dominated, double peak at  $+0.8$  eV (of mainly  $d_{(xz,yz)}$  symmetry) and at  $+1.6$  eV (of mixed  $d$  symmetry); (iii) a sharp positive peak, of mainly Ti and Si  $p$  character, at  $-1.0$  eV; (iv) a smaller positive peak, of

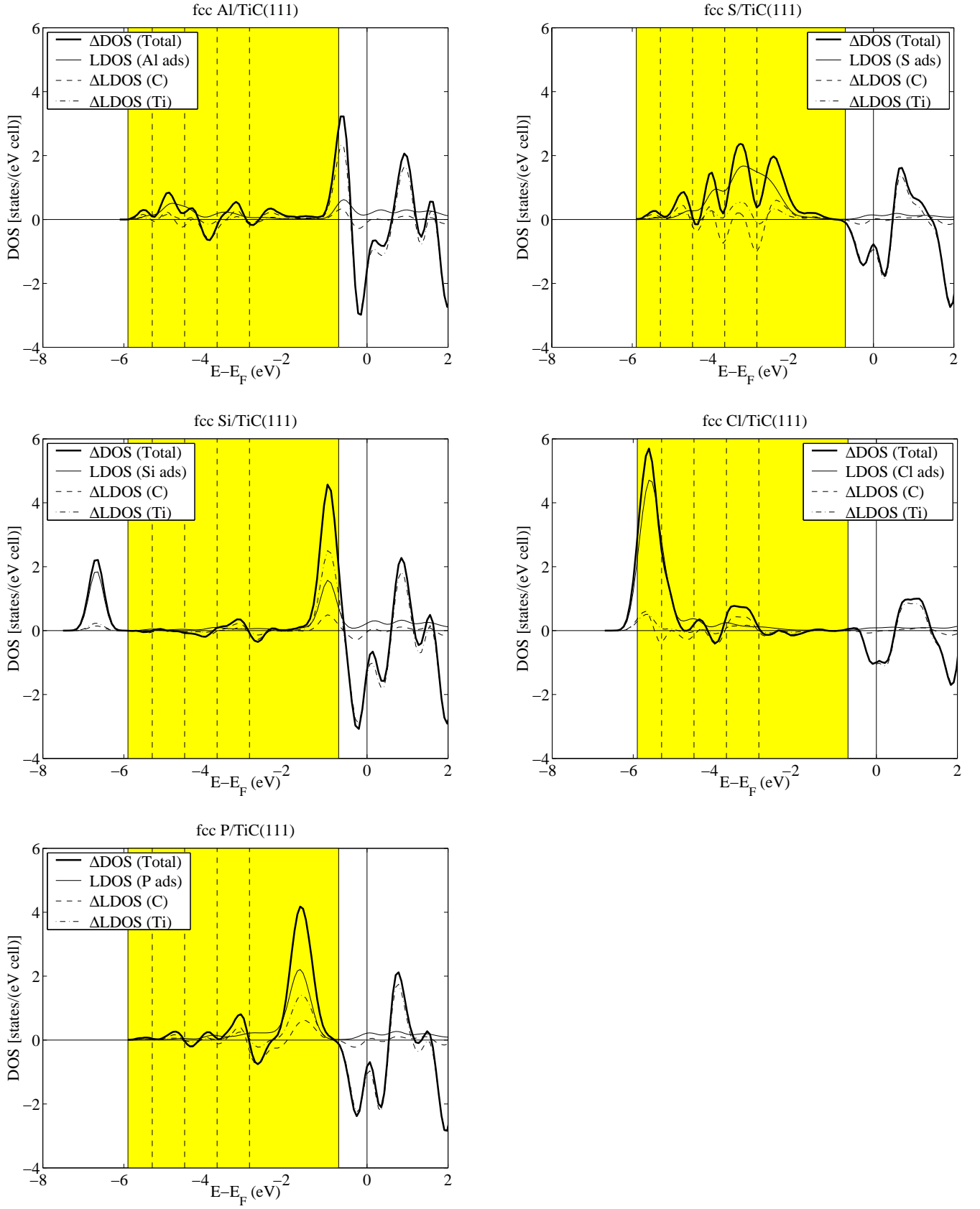


FIG. 20: Same as Fig. 14 but for the third-period elements Al, Si, P, S, and Cl.



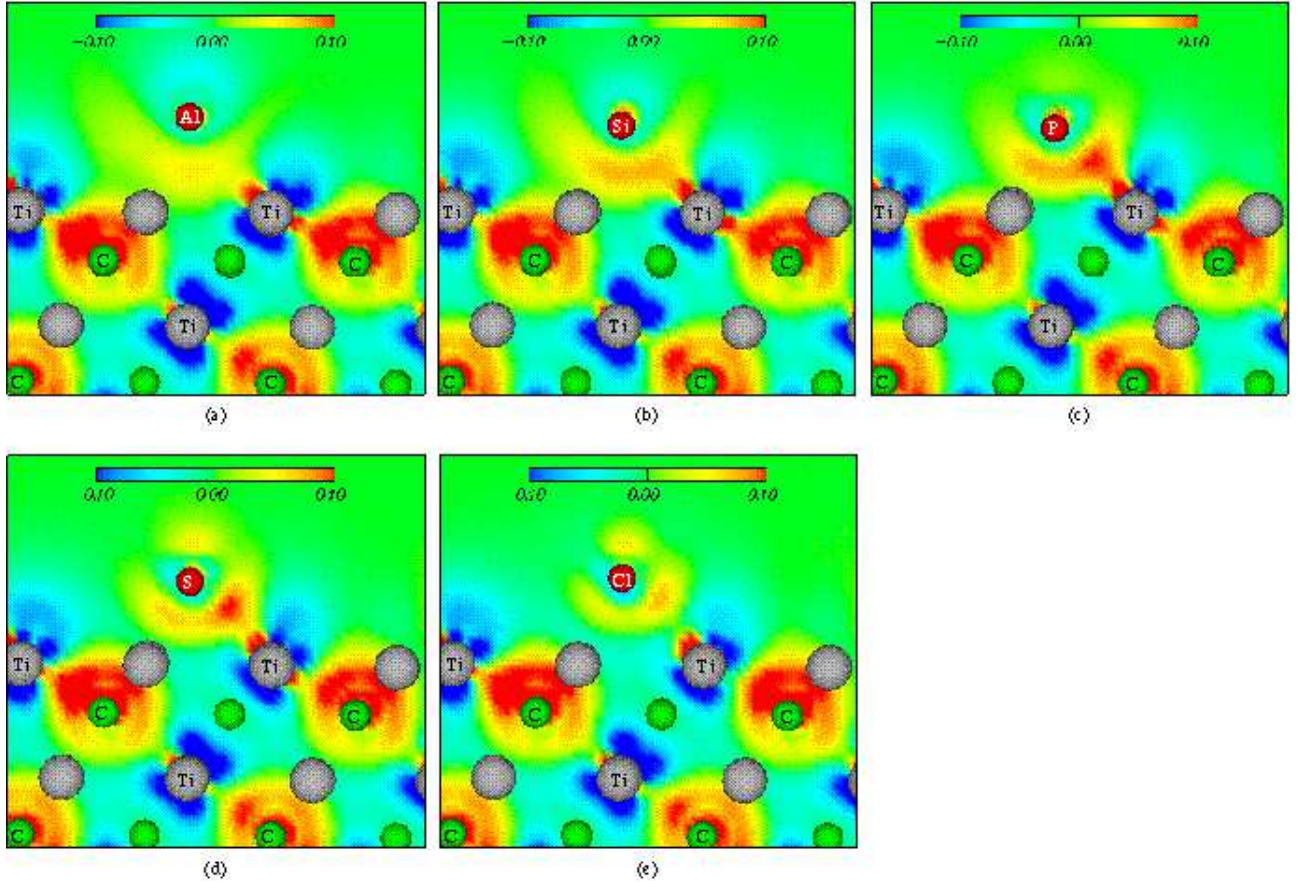


FIG. 21: (Color online). Same as Fig. 16 but for the systems with the third-period adatoms (a) Al, (b) Si, (c) P, (d) S, and (e) Cl adsorbed in fcc site on the TiC(111) surface.

almost exclusively Si  $s$  character, at  $-6.6$  eV; (v) much smaller negative peaks at  $-4.0$  and  $-2.7$  eV, of mainly C character; (vi) a small positive peak at  $-3.2$  eV, of mainly C character.

The DOS( $\mathbf{r}, E$ ) plots show that (i) very strong Si–Ti bonding states are present around  $-1.0$  eV; (ii) the states at  $-6.6$  eV are almost exclusively Si centered, although some weak Si–Ti bonding overlap can be detected; (iii) almost no Si-centered states are found around the smaller negative and positive peaks; (iv) the negative-peak region just below  $E_F$  corresponds again to a depletion of the TiSR around the Si adatom.

The total electron-density plot for Si [Fig. 21(b)] is similar to that for Al, with a strong polarization toward the substrate and in particular toward the NN Ti atoms. Compared to Al, the electron transfer from the surface-bilayer Ti and C atoms to the Si adatom is larger, yielding a Si adatom ionicity of  $-0.93|e|$ . This is clearly visible in the electron-density plot, showing a higher electron density in the region below the Si adatom than below the Al adatom.

P adatom: For P, the  $\Delta$ DOS( $E$ ) (Fig. 20) shows (i) again a negative, Ti-dominated, double-peak structure at  $-0.3$  and  $+0.3$  eV, with same orbital symmetries as for Al

and Si but with weaker low-energy peak than for Al and Si; (ii) a positive, Ti-dominated, double peak at  $+0.8$  eV (of mainly  $d_{(xz,yz)}$  symmetry) and at  $+1.5$  eV (of mixed  $d$  symmetry); (iii) a main positive peak, slightly broader than for Si and of mainly P  $p$  and Ti character, at  $-1.6$  eV; (iv) smaller positive peaks, of mainly C character, at  $-3.1$ ,  $-3.9$ , and  $-4.7$  eV; (v) small negative peaks, of mainly C character, at  $-2.7$  and  $-4.4$  eV.

The DOS( $\mathbf{r}, E$ ) plots show (i) very strong P–Ti bonding states around the main peak; (ii) weak P–C and P–Ti bonding states around the peaks at  $-3.1$  and  $-3.9$  eV; (iii) weak P–Ti bonding overlap around  $-4.7$  eV; (iv) a depletion of the TiSR around P and a weak P-centered dangling bond in the negative-peak region just below  $E_F$ .

The total electron-density plot for P [Fig. 21(c)] is similar to those for the previous third-period adatoms, with a strong polarization toward the substrate and in particular toward the NN Ti atoms. However, the charge density around the P adatom is much higher than around Al and Si. This is reflected by the Bader charges (Table IV), yielding a stronger electron transfer from the surface-bilayer atoms to the P adatom than to Al and Si, the P adatom ionicity being  $-1.12|e|$ .

S adatom: For S, the  $\Delta$ DOS( $E$ ) (Fig. 20) resem-

bles that for N and shows (i) the usual negative, Ti-dominated, double-peak structure at  $-0.3$  and  $+0.3$  eV, with the same orbital symmetries as for Al, Si, and P, but with weaker peaks than for Al, Si, and P; (ii) a Ti-dominated double peak above  $E_F$ , smaller than for previous third-period adatoms and composed of a main peak at  $+0.7$  eV (of mainly  $d_{(xz,yz)}$  symmetry) and of a secondary peak around  $+1.1$  eV (of mixed  $d$  symmetry); (iii) a broad positive region between  $-5.9$  and  $-0.9$  eV, which, similarly to N, is composed of five peaks (at  $-5.4$  and  $-4.7$  eV, which show mainly C character, and at  $-4.0$ ,  $-3.3$ , and  $-2.5$  eV, which show mainly S  $p$  character).

The DOS( $\mathbf{r}$ ,  $E$ ) plots show that (i) the region below  $-3.8$  eV is dominated by S–C bonding states, with weaker S–Ti contributions; (ii) the region around  $-3.3$  eV shows equally strong amounts of S–C and S–Ti bonding states; (iii) the region above  $-3.2$  eV displays only S–Ti bonding states; (iv) the negative-peak region just below  $E_F$  is characterized by a depletion of the TiSR around S and by a weak S-centered dangling bond, slightly stronger than in the case of P.

The total electron-density plot for S [Fig. 21(d)] shows similarities to those for the previous third-period adatoms. However, the electron density around the S adatom, although still strongly polarized toward the NN Ti atoms, is smaller than for the previous third-period adatoms. This is reflected by the smaller electron transfer from the surface-bilayer Ti and C atoms to the S adatom, compared to the previous third-period adatoms, as obtained from the Bader charges (Table IV), which yield a S adatom ionicity of  $-1.06|e|$ .

Cl adatom: For Cl, finally, the  $\Delta$ DOS( $E$ ) (Fig. 20) shows (i) again a negative double peak around  $E_F$  (at  $-0.1$  and  $+0.2$  eV), much smaller than for the other third-period adatoms but with the same Ti  $d$  symmetries; (ii) a positive double peak above  $E_F$  (at  $+0.8$  and  $+1.1$  eV, both with mainly Ti  $d_{(xz,yz)}$  symmetry); (iii) a main positive peak at  $-5.6$  eV, with an almost exclusively Cl  $p$  character; (iv) smaller positive peaks at  $-4.4$  eV (of predominantly Cl  $p$  character), and at  $-3.5$  and  $-3.3$  eV (of mainly C character); (v) a small negative peak, of mainly C character, at  $-4.0$  eV.

The DOS( $\mathbf{r}$ ,  $E$ ) plots show that (i) the main peak consists of mainly Cl-centered states, which nevertheless form strong bonding coupling to neighboring C and Ti atoms; (ii) the states around  $-4.4$  eV show weak Cl–Ti bonding coupling; (iii) all other states show little or no Cl contribution; (iv) the negative-peak region just below  $E_F$  is again characterized by a depletion of the TiSR around the Cl adatom and by a weak Cl-centered dangling bond, stronger than for the previous third-period adatoms.

The total electron-density for Cl [Fig. 21(e)] shows a significantly smaller electron density around the adatom, compared to the other third-period adatoms. Almost zero electron-density difference is found in between the Cl adatom and its NN Ti atoms, indicating an ionic bond. Indeed, the Bader analysis (Table IV) yields an almost

completely ionized Cl adatom, its ionicity being  $-0.75|e|$ .

(d) *O adatom in hcp and top sites on TiC(111).* In order to understand whether the nature of the adsorption is affected by the adsorption site, we also calculate and examine the electronic structures of the most stable adatom, O, in hcp and top sites and compare them to the results for O in fcc site.

O adatom in hcp site: The  $\Delta$ DOS( $E$ ) for an O adatom adsorbed in the hcp site on the TiC(111) surface [Fig. 22(a)] shows that (i) the negative, Ti-dominated, double peak around  $E_F$  (at  $-0.2$  and  $+0.1$  eV, of  $d_{(xz,yz)}$  +  $d_{(xy,x^2-y^2)}$  and  $d_{(xz,yz)}$  symmetry, respectively) is considerably smaller than in the  $\Delta$ DOS for the fcc O adatom; (ii) the positive, Ti-dominated, positive peak at  $+0.6$  eV (of  $d_{(xy,x^2-y^2)}$  symmetry) is also considerably smaller than for fcc O; (iii) an additional negative peak, of mainly C  $p_z$  character, is present at  $-2.8$  eV; (iv) the main positive peak, mainly composed of O  $p_{xy}$  states, with a smaller contribution from O  $p_z$  states, lies at  $-4.9$  eV; (v) smaller positive peaks are present at  $-4.3$  and  $-3.7$  (of mainly  $Op_z$  character) and at  $-2.3$  and  $-1.6$  eV (of mainly mixed O  $p_z$  and C  $p_z$  character); (vi) there is a shoulder on the low-energy side of the main peak, caused by a positive peak of C  $p$  symmetry located at  $-5.5$  eV.

The DOS( $\mathbf{r}$ ,  $E$ ) plots show that (i) the main peak is composed of strong O–C and O–Ti bonding states; (ii) the low-energy shoulder of the main peak is dominated by very strong O–C bonding states; (iii) the peak at  $-4.3$  eV contains both O–Ti and O–C bonding states; (iv) only O–Ti bonding states are found around the remaining positive  $\Delta$ DOS peaks; (v) the region of the negative peak just below  $E_F$  consists of a depletion of the TiSR around the O adatom and of a small O-centered dangling bonds [Fig. 23(a)].

O adatom in top site: The  $\Delta$ DOS( $E$ ) for an O adatom adsorbed in the top site on TiC(111) [Fig. 22(b)] shows that (i) the negative, Ti-dominated, double peak around  $E_F$  (at  $-0.2$  and  $+0.4$  eV, of essentially the same symmetries as for hcp O, although a slightly larger  $d_{z^2}$  contribution is present for the peak at  $-0.2$  eV), is again considerably smaller than for the fcc O adatom; (ii) the positive, Ti-dominated, peak at  $+0.9$  eV (of mainly  $d_{(xz,yz)}$  symmetry) has a similar height as the corresponding peak for fcc O; (iii) the main positive peak (of mainly O  $p_{xy}$  character) lies at a considerably higher energy than for fcc and hcp O, at  $-3.3$  eV; (iv) other positive peaks are present at  $-5.5$  and at  $-4.7$  (of mainly C character), and at  $-2.5$  eV (of mainly O  $p_z$  character); (v) there is a shoulder on the low-energy side of the main peak, caused by a C-centered peak located at  $-4.0$  eV.

The DOS( $\mathbf{r}$ ,  $E$ ) plots show almost exclusively O–Ti bonding states. Still, a clear O–C coupling is present at the low-energy shoulder of the main peak, at  $-4.0$  eV, and a weaker O–C coupling is present at the main peak, at  $-3.3$  eV. The sum of the DOS( $\mathbf{r}$ ,  $E$ ) for all occupied states above  $-0.3$  eV [Fig. 23(b)] shows that the top O adatom causes a depletion of the TiSR in the three neighboring fcc sites. As opposed to fcc and hcp O,

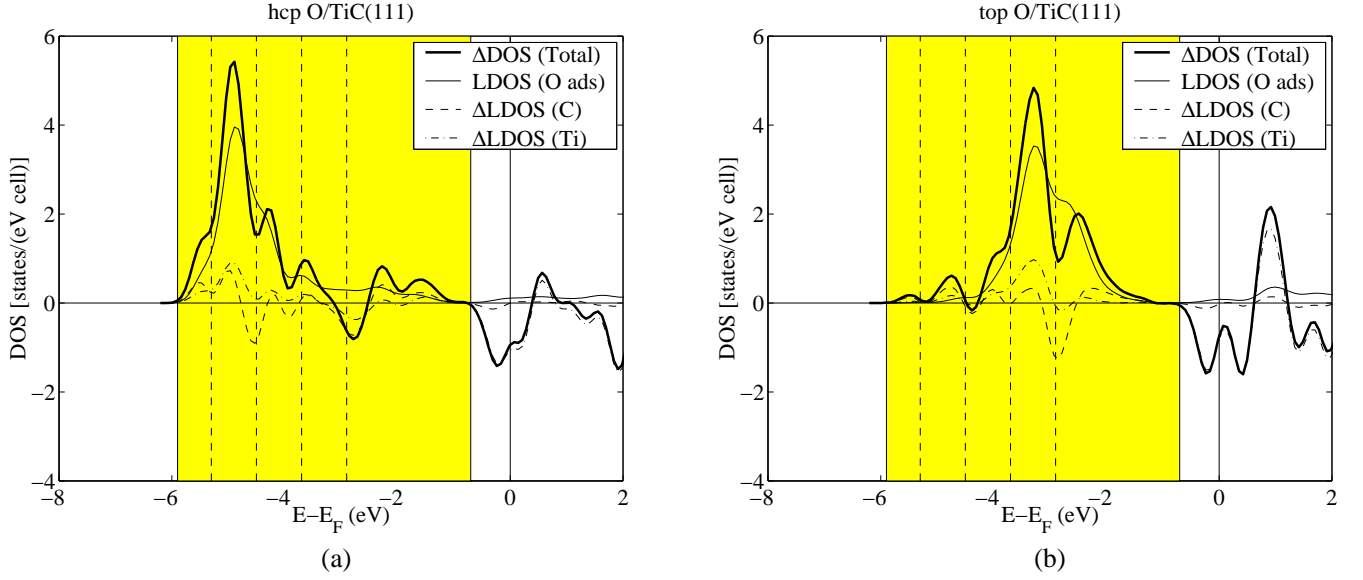


FIG. 22: Same as Fig. 14 but for an O atom adsorbed in (a) the hcp site and in (b) the top site on the TiC(111) surface.

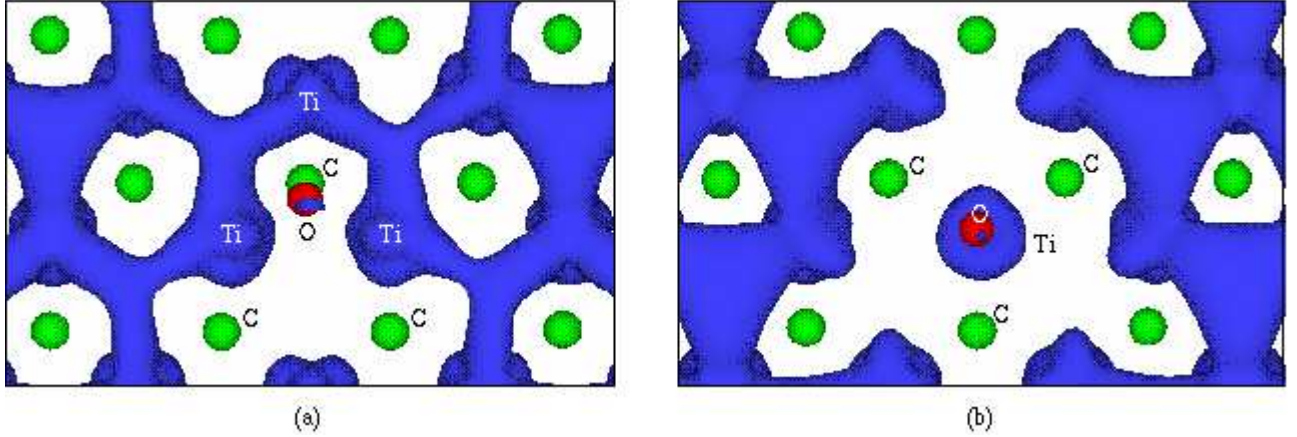


FIG. 23: Same as Fig. 15(c) but for an O atom adsorbed in (a) the hcp site and in (b) the top site on the TiC(111) surface. The contour plots correspond to the same value of the  $\text{DOS}(\mathbf{r}, E)$  as the contour plot in Fig. 19.

however, the TiSR is non-vanishing directly below the O adatom, due to the presence of the nearest-neighbor Ti atom.

(e) *O adatom on TiC(001)*. For comparison, the electronic structure for O on TiC(001) is also examined.

The  $\Delta\text{DOS}(E)$  for an O adatom adsorbed in the on-top-C site of the TiC(001) surface (Fig. 24) is characterized by (i) a strong negative peak, of predominantly C character, at  $-1.5$  eV; (ii) a positive double-peak structure, of mainly O and C character, at  $-6.3$  and  $-5.9$  eV (orbital projection reveals that the more bound peak, at  $-6.3$  eV, consists of O and C states with exclusively  $p_{xy}$  symmetry, while the peak at  $-5.9$  eV shows only  $p_z$  symmetry); (iii) smaller positive peaks, of mixed adatom and substrate character, at  $-3.7$ ,  $-2.8$ , and  $-2.2$ ; (iv) an O-dominated positive peak at  $-0.6$  eV; (v) small positive

peaks, of mainly Ti character, above  $E_F$  (at  $+0.2$ ,  $+0.7$ , and  $+1.4$  eV).

### 3. Analysis of the Electronic Structure: The Concerted-Coupling Model

In this subsection, the above-described electronic structure results for the atomic adsorption on TiC(111) are analyzed and interpreted in terms of the Newns-Anderson (NA) chemisorption model. This yields a model for the nature of the chemisorption on TiC(111) that we call the “concerted-coupling model”, since it describes the adatom-substrate interaction as arising from the concerted action of two contributions: (i) a strong, in the NA sense, coupling between the adatom state(s)

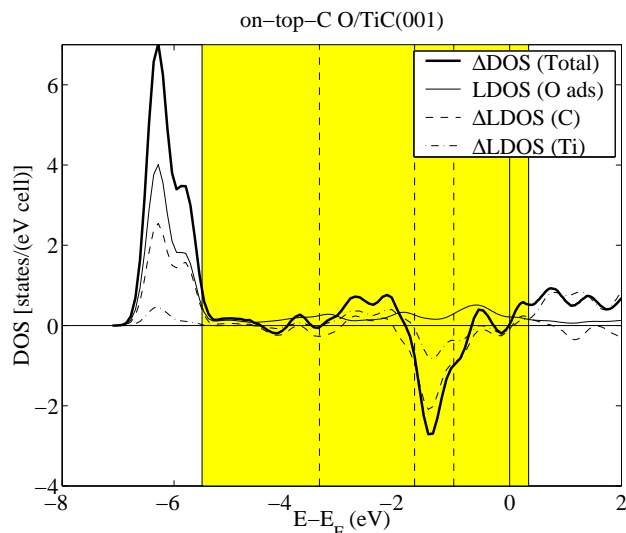


FIG. 24: Same as Fig. 14 but for an O atom adsorbed in the on-top-C site on the TiC(001) surface.

and the substrate TiSR, and (ii) a coupling, whose strength varies between the different adatoms, between the adatom state(s) and the substrate CSR's.

First [Sec. III.C.3(a)], the essential points of the NA model are briefly summarized, providing a theoretical framework for our subsequent analysis of the electron-structure results for fcc H on TiC(111) [Sec. III.C.3(b)]. A model for the nature of the H-TiC(111) interaction is thus proposed. Then [Secs. III.C.3(c)–(f)], this model is successfully applied to the description of our electron-structure results for the other systems described in Sec. III.C.2. Thus, we conclude that this model is suited for a general description of the nature of chemisorption on TiC(111). In Sec. III.D, the model is also shown to yield a good description of the chemisorption of a full ( $1 \times 1$ ) monolayer of O on TiC(111). In Sec. IV, the energetical consequences of the model are discussed in a qualitative way. By correlating the trends in electronic structures with the trends in calculated adsorption energies, we point out which features of the concerted-coupling model are important for the chemisorption strength on TiC(111).

(a) *The Newns-Anderson (NA) model for chemisorption.* In the NA model,<sup>66</sup> chemisorption on metal surfaces is described with a Hamiltonian originally introduced for the description of magnetic impurities.<sup>67</sup> The solutions to the NA Hamiltonian provide a theoretical framework for the description of the basic mechanisms behind chemisorption on metal surfaces. It has been used, for example, to successfully describe chemisorption trends on transition-metal surfaces (the *d*-band model).<sup>69,70,71</sup>

Here, the basic concepts arising from the NA model are presented. These are then used in our analysis of the electron-structure results for chemisorption on TiC(111).

Traditionally, two limiting cases are considered in the solution of the NA Hamiltonian: “weak” and “strong”

chemisorption.<sup>66,68</sup>

In the weak limit, the coupling matrix element between adatom and substrate states is small compared to the width of the substrate band. A single solution is thus obtained,  $E \approx \varepsilon_a^* + \Lambda(\varepsilon_a^*)$ , where  $\varepsilon_a^*$  is the effective atomic level of the adatom (that is, the free atomic level shifted due to the electrostatic interaction of the adatom with the metal surface), and  $\Lambda(\varepsilon_a^*)$  is small compared to the substrate band width. If  $E$  falls within the energetical region of the substrate band, the resulting adsorbate level is broadened. Otherwise, the resulting DOS consists of a single state outside the substrate energy band, together with a typically small and continuous contribution extending over the whole substrate band.

In the strong limit, the adatom–substrate coupling matrix element is large compared to the substrate band width. This yields three solutions to the NA Hamiltonian: two single states, one on each side of the substrate band, together with a weak continuous part extending over the whole substrate band. These two single states can be regarded as the “bonding” and “antibonding” states, respectively, of a “surface molecule” formed by the adatom and its neighboring substrate atoms.

By applying the NA model in a tight-binding approximation, Ref. 68 shows that these bonding and antibonding states appear gradually with increasing size of the ratio  $\beta'/\beta$ , where  $\beta'$  is the adatom–substrate hopping integral and  $\beta$  is the substrate hopping integral. At small  $\beta'/\beta$  values, the coupling is weak and the adsorbate level is broadened. As  $\beta'/\beta$  increases, this level broadens further and splits gradually into two separate levels.

In addition to the weak and strong chemisorption, it is therefore reasonable to speak also of an “intermediate” chemisorption, in which the adsorbate level is strongly broadened and split into bonding and antibonding subpeaks. The stronger the chemisorption is, the more are these subpeaks separated from one another.

(b) *H adatom in fcc site on TiC(111).* The  $\Delta\text{DOS}(E)$  for fcc H on TiC(111) (Fig. 14) shows a strong negative peak in the energetical region of the TiSR. This indicates that the adsorption of H causes a strong quenching of the TiSR around the adatom, a fact confirmed by our real-space visualization of the states in this energetical region [Fig. 15(c)]. Thus, the TiSR participates in the formation of adatom–substrate bonds. Since the TiSR is rather sharp, having weak dispersion and being well localized around the surface Ti atoms [Sec. III.B.2(a)], the coupling between the adatom state and the TiSR can be expected to be strong, in the NA sense, and should therefore give rise to well separated bonding and antibonding surface-molecule states (Fig. 25). The bonding state should lie below the atomic level of the adatom and the antibonding state should lie above the TiSR energy.

Indeed, the  $\Delta\text{DOS}(E)$  shows the appearance of a positive peak above the TiSR and of a broad positive region below it. The peak above the TiSR can thus be interpreted as the antibonding adatom–TiSR state, while the positive region below the TiSR can be interpreted as



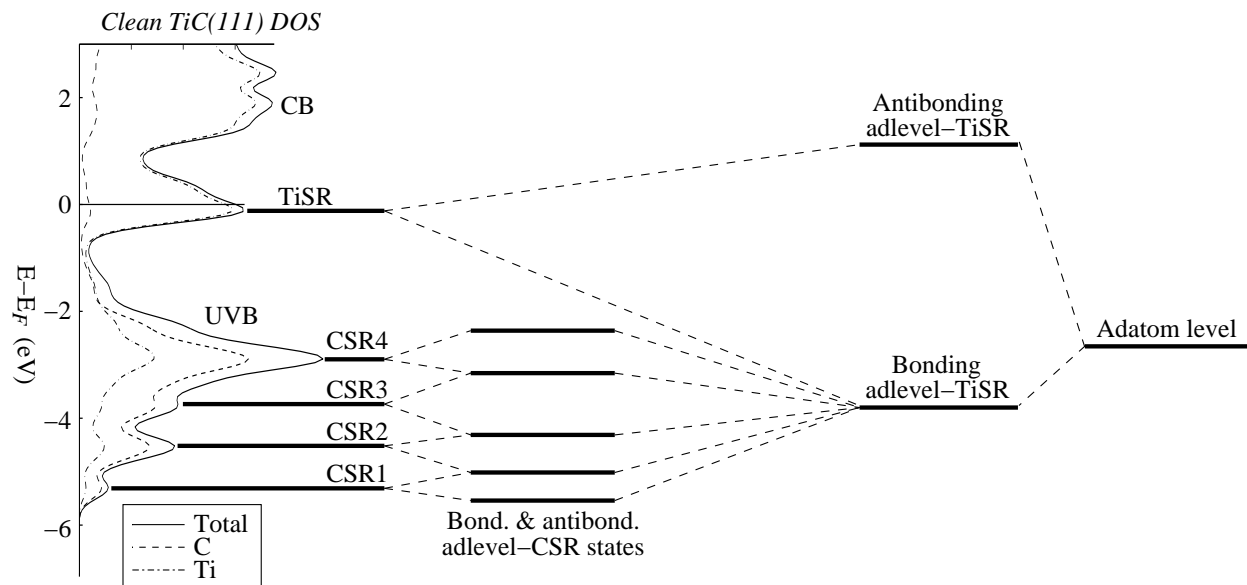


FIG. 25: Schematic diagram of the concerted coupling between the adatom state and the TiC(111) Ti- and C-centered surface resonances (TiSR and CSR1–CSR4).

bonding adatom–TiSR states.

At the same time, the adatom level can also be expected to hybridize with the substrate UVB states, in a way similar to the weak coupling to the  $sp$  band on transition-metal surfaces.<sup>69,71</sup> On TiC(111), however, such an interaction should be stronger than on pure transition metals, due to the more localized nature of the TiC(111) UVB, compared to the transition-metal  $sp$  band. Indeed, our  $\Delta\text{DOS}(E)$  shows a strong negative peak at the energetical location of one of the TiC(111) UVB peaks, indicating a strong coupling between this peak and the adatom state. As shown in Sec. III.B.2(b), this UVB peak (called CSR3 in Fig. 6) corresponds to surface-localized C states, or CSR’s. Indeed, the negative  $\Delta\text{DOS}$  peak is mainly localized around the surface-layer C atoms.

Furthermore, a closer inspection of the  $\Delta\text{DOS}$  reveals that negative, C-centered, peaks are also present at the energetical locations of the two lowest TiC(111) UVB peaks, CSR1 and CSR2, and that the energies of the positive peaks lie in-between the energies of the UVB peaks. Thus, this indicates that the adatom level couples rather strongly with the TiC(111) CSR’s, giving rise to bonding and antibonding states that combine to form the observed positive  $\Delta\text{DOS}$  peaks (Fig. 25).

According to this interpretation, the low-energy  $\Delta\text{DOS}$  peaks should be characterized by bonding adatom–C states, while the high-energy peaks should lack such states. Our  $\text{DOS}(\mathbf{r}, E)$  plots confirm this: at lower energies, bonding adatom–C states dominate over adatom–Ti states [Fig. 15(a)]; as the energy increases, this adatom–C character diminishes in favor of the bonding adatom–Ti

states; above the main negative  $\Delta\text{DOS}(E)$  peak, only adatom–Ti states are found [Fig. 15(b)].

Our electron-structure results for fcc H on TiC(111) indicate therefore that the chemisorption arises from the concerted action of two different types of adatom–substrate couplings: (i) a strong coupling between the adatom state and the TiSR and (ii) a somewhat weaker coupling between the adatom state and the CSR’s that are present in the low-energy part of the TiC(111) UVB. We call this a *concerted coupling*. This mechanism has similarities to the  $d$ -band model for chemisorption on transition metals.<sup>69,70,71</sup> Here, however, the weak coupling to the  $sp$  band is replaced by a stronger coupling to the more localized TiC(111) CSR’s, increasing the importance of this coupling for the chemisorption strength. In particular, the following analyses show that the strength of this coupling varies significantly between the different adatoms and can therefore be expected to play a role in the chemisorption-strength trends.

In order to analyze these variations and trends, we now turn to the analysis of the electronic structures for the second- and third-period adatoms and of whether the concerted-coupling model is valid also for these adatoms, which are characterized by frontier orbitals of  $p$  symmetry, in contrast to the simpler  $s$  symmetry of the H orbital.

(c) *Second-period adatoms in fcc site on TiC(111)*. Like for H, the  $\Delta\text{DOS}$ ’s for the second-period adatoms in fcc site on TiC(111) (Fig. 17) show a strong negative peak in the energetical region of the TiSR, together with positive peak(s) just above the TiSR and regions of sharp or broadened positive peaks below it. Thus, also

for the second-period adatoms, there is a strong coupling between the adatom state and the TiSR. The area of the negative  $\Delta$ DOS peak increases slightly as  $B \rightarrow C$  and decreases as  $C \rightarrow N \rightarrow O \rightarrow F$ , indicating corresponding increase and decreases, respectively, of the adatom–TiSR coupling strength.

The energetical region above the TiSR looks generally similar for all second-period adatoms, with a Ti-centered positive single- or double-peak around  $\sim +1.0$  eV. Like for H, this can be interpreted as the antibonding solution of the adatom–TiSR coupling. On the other hand, the positive region below the TiSR, which can correspondingly be interpreted as composed of bonding adatom–TiSR states, differs between the different adatoms. For all adatoms, it contains a positive region characterized by states of mixed substrate-Ti  $d$ , substrate-C  $p$ , and adatom  $p$  symmetries. This region is successively shifted to lower energies as the adatom nuclear charge  $Z$  increases. This shift agrees with the interpretation of this region as the bonding solution of the adatom–TiSR coupling. Such a bonding solution must lie below the energy of the free adatom state. As  $Z$  increases, the valence electrons of the free adatom are more strongly bound to its nucleus, that is, their energies are lowered. As the free-adatom state decreases in energy, so must also the bonding solution of the adatom–TiSR coupling.

As  $Z$  increases, the bonding adatom–TiSR state overlaps therefore with different parts of the substrate electronic structure, at successively decreasing energies. In particular, our calculated  $\Delta$ DOS’s show that: for B, it lies at the upper edge of the substrate UVB region and is very sharp; for C, it lies in the high-energy region of the UVB and is slightly broadened; for N, it lies in the middle of the UVB region and is strongly broadened and split into subpeaks; for O, it lies in the low-energy region of the UVB and is broadened and somewhat split into subpeaks; and for F, it lies well below the UVB region and is very sharp. In addition, our DOS( $\mathbf{r}$ ,  $E$ ) plots show that, for all adatoms, only adatom–Ti bonding states are present in the high-energy region of the UVB, while both adatom–Ti and adatom–C bonding states are present in the middle- and low-energy regions of the UVB, and that the adatom–C contribution increases successively as the energy decreases.

Thus, the strength and nature of the coupling between the adatom and the TiC(111) UVB states vary significantly between the different adatoms. For B, the sharpness of the positive  $\Delta$ DOS peak indicates that it only corresponds to bonding adatom–TiSR states [as confirmed by the DOS( $\mathbf{r}$ ,  $E$ ) plots] and that no coupling takes place with the UVB states.

For C, the positive  $\Delta$ DOS peak is slightly broadened, indicating a weak coupling of the adatom state to the states in the upper region of the UVB. Since these states are Ti-dominated [see Sec. III.B.2(b)], no strong adatom–C bonds are formed. However, a small subpeak is formed just below the main UVB peak, containing very weak adatom–C bonding states. This indicates a very weak hy-

bridization with the C-centered states of the main UVB peak.

For N, the strong broadening and partial splitting of the positive  $\Delta$ DOS peak indicate a rather strong adatom–UVB coupling. Like for the fcc H adatom, positive peaks are formed in between the peaks of the substrate-UVB DOS. At the same time, negative C-localized peaks are present at the energies of the substrate UVB peaks, indicating that the CSR’s in the substrate UVB hybridize with the adatom state. The formation of subpeaks in the positive  $\Delta$ DOS can therefore be interpreted as the formation of bonds between the adatom and the C atoms in the surface TiC bilayer. Similarly to the case of the H adatom, these subpeaks correspond to combinations of bonding and antibonding adatom–C states. This is confirmed by the DOS( $\mathbf{r}$ ,  $E$ ) plots, which show a successively stronger dominance of bonding adatom–C states with decreasing energy, as well as the absence of any bonding adatom–C states at energies higher than the main substrate-UVB peak (CSR4).

At the same time, the differences between the N and H  $\Delta$ DOS’s can be attributed to the different symmetries of the adatom valence states ( $s$  for H and  $p$  for N). For example, the much stronger coupling to the TiSR for N (as well as for the other second- and third-period adatoms) than for H (illustrated by the much stronger negative  $\Delta$ DOS peaks around  $E_F$  for N) can be understood from the better spatial overlap of the TiSR  $d_{xz,yz} + d_{xy,x^2-y^2}$  orbitals with the  $p$  (mainly, the  $p_{xy}$ ) orbitals of the second- and third-period adatoms than with the  $s$  orbital of the H adatom.

For O, the splitting of the positive  $\Delta$ DOS peak indicates again an adatom–UVB coupling. Like for N, positive subpeaks are present in between the substrate-UVB peaks, while negative, C-localized, peaks are present at the energies of the UVB peaks. As described in Sec. III.C.2(b), the main, broad, O  $p$  peak, which straddles the lowest-energy UVB peak, is actually composed of an O  $p_{xy}$  peak and of an O  $p_z$  peak, each lying on opposite sides of the lowest-energy UVB peak. Therefore, also for O, the  $\Delta$ DOS can be interpreted as evidence for rather strong hybridizations between the adatom state and the CSR’s. In particular, the main positive  $\Delta$ DOS peaks lie here in the UVB region that is dominated by the CSR’s, that is, below the main peak (CSR4) of the substrate UVB. As our DOS( $\mathbf{r}$ ,  $E$ ) plots show, it is in this region that the strongest bonding adatom–C states are found.

It is also interesting to notice that the most strongly bonding O–C states have O  $p_{xy}$  symmetry. This agrees with the experimental findings for full ( $1 \times 1$ ) monolayer coverage of O on TiC(111) [see Sec. III.C.2(b)].<sup>28</sup> Apparently, the stronger bonding of the O  $p_{xy}$  orbitals, compared to the O  $p_z$  orbitals, is due to the geometry of the fcc site, which favors lateral ( $xy$ ) interaction with both the Ti and the C atoms of the TiC(111) surface bilayer.

Finally, for F, the sharpness of the positive  $\Delta$ DOS peak shows that no adatom–UVB coupling occurs, due to the fact that the adatom level lies well outside the energetical



region of the UVB.

Thus, like for the fcc H adatom, two different types of couplings can take place also for the second-period adatoms: one between the adatom state and the substrate TiSR and one between the adatom state and the substrate CSR's. However, their strengths vary significantly with varying  $Z$  within the adatom period. In particular, the strength of the coupling to the CSR's varies from no coupling (B and F) to rather strong coupling (O and N).

Finally, we note that, for B, the B  $s$  state lies in the low-energy region of the substrate UVB. This causes a slight broadening of the B  $s$  level, as well as the formation of a weak subpeak slightly above the main B  $s$  peak. The DOS( $\mathbf{r}$ ,  $E$ ) plots show that, like for the adatom  $p$  states, this is due to a hybridization between the adatom  $s$  state and the CSR's of the surface TiC bilayer.

(d) *Third-period adatoms in fcc site on TiC(111)*. The calculated electronic structures for the third-period adatoms in fcc site on TiC(111) show trends that are very similar to those for the second-period adatoms. Overall, however, two main differences can be detected: (i) the negative  $\Delta$ DOS peak is smaller than for the second-period adsorbates and (ii) the positive  $\Delta$ DOS peak below the TiSR lies at higher energies than for the second-period adsorbates. Both differences are due to core orthogonalization, (i) resulting from the larger radii of the third-period adatoms, which cause smaller overlaps between adatom and TiSR wavefunctions and thus weaker adatom-TiSR couplings and (ii) from the higher energy, within a group, of the valence electron state of a free third-period atom.

Still, however, the two types of couplings described above are present. Like for the second-period adatoms, the adatom-TiSR coupling strength appears to slightly increase as Al  $\rightarrow$  Si and to decrease as Si  $\rightarrow$  P  $\rightarrow$  S  $\rightarrow$  Cl. The coupling between the adatom  $p$  state and the CSR's follows also a similar trend as for the second-period adatoms, however, with differences due to the higher free-adatom energy levels. The coupling to the UVB is now very weak for both Al and Si, both with positive  $\Delta$ DOS peaks around the top of the substrate-UVB region. The  $\Delta$ DOS for P resembles that for C, the slightly lower energy of the P peak, however, causing a slightly stronger adatom-UVB coupling, shown by the slightly stronger peak broadening and the formation of a low-energy subpeak with slightly stronger adatom-C bonding character. In the same way, the  $\Delta$ DOS for S resembles that for N, with strong subpeaks formed by the hybridization between the adatom state and the CSR's.

For Cl, the main positive  $\Delta$ DOS peak lies in the low-energy region of the substrate UVB, at a slightly lower energy than that of the O main peak. Thus, the Cl state might be expected to behave similarly to the O state and couple strongly to the CSR's. However, our calculated  $\Delta$ DOS's show a smaller broadening and subpeak formation for Cl than for O. Further, the DOS( $\mathbf{r}$ ,  $E$ ) plots show that the Cl peak is composed of states that

are strongly localized around the Cl adatom, with a very weak coupling to substrate atoms. The adatom-UVB coupling is thus much weaker for Cl than for O. The reason is clearly seen in our Bader calculations of the atomic charges (Table IV). For all adatoms, electrons are transferred from the surface-bilayer Ti and C atoms to the adatom. For the group-VII elements (F and Cl) this transfer is large enough to almost completely fill the outer valence-electron shell of the adatom, thus almost completely ionizing these adatoms. This is confirmed by our analysis of the total electronic density around each adatom (see Sec. III.C.2 and Figs. 18 and 21), which shows an increase in electron density along the adatom-Ti bond for all adatoms except for F and Cl. This is indicative of covalent adatom-Ti bonds for all adatoms except for F and Cl, which show a prevalently ionic type of bond. The almost filled valence-electron shell of Cl is therefore almost inert toward further hybridization with the CSR's, resulting in a weaker adatom-UVB coupling than in the case of O.

Thus, also for the third-period adatoms, chemisorption is characterized by the concerted action of the two different types of coupling: adatom-TiSR and adatom-CSR's. Again, within the period, the coupling strengths vary significantly with  $Z$ . In addition, they differ between the two periods, due to the extra electron shell in period three.

Finally, it can be noted that for Al, the adatom  $s$  state lies inside the energetical region of the substrate UVB and is therefore broadened and split into subpeaks of adatom-C and adatom-Ti bonding character.

(e) *O adatom in hcp and top sites on TiC(111)*. In order to test whether the concerted-coupling model can also be used to understand our results for adsorption in other sites than fcc, we now analyze the electronic structures for the O adatom in hcp and top sites.

For both hcp and top O adatom, the  $\Delta$ DOS's show negative peaks in the energetical region of the TiSR, together with positive peaks just above and broader positive regions below. Thus, the coupling to the TiSR is active in these adsorption sites as well. However, for both hcp and top O, the resulting bonding states (*i.e.*, the positive  $\Delta$ DOS region below the TiSR) lie at higher energies than for fcc O, implying a weaker adatom-TiSR coupling.

For the hcp adatom, the reason for this can be found in the symmetry of the TiSR. As shown in Sec. III.B.2(a), due to its dangling-bond character, the TiSR extends toward the fcc site and avoids the hcp site. Thus, the overlap between the adatom states and the TiSR is smaller in the hcp site than in the fcc site, resulting in a weaker hopping integral  $\beta'$  between the adatom and its NN Ti atoms.

This is confirmed by our DOS( $\mathbf{r}$ ,  $E$ ) plots for the energetical region of the TiSR, which show that also for the hcp O adsorbate [Fig. 23(a)], the TiSR depletion occurs around the fcc site close to the adatom. Also, the relaxation displaces the hcp adatom slightly toward the

neighboring fcc site, indicating that the adatom–TiSR hybridization is stronger in the fcc site.

As described in Sec. III.C.3(a), the degree of broadening of the adsorbate level and of its splitting into bonding and antibonding states depends on the strength ratio  $\beta'/\beta$ , where  $\beta$  is the substrate hopping integral.<sup>68</sup> A smaller value of  $\beta'/\beta$  implies a smaller splitting. Thus, the weaker adatom–TiSR overlap in the hcp site, compared to the fcc site, causes a smaller downward shift of the resulting bonding-state energy from the free adatom-state energy. Indeed, the main positive peak below the TiSR in the hcp  $\Delta$ DOS lies 0.6 eV higher than in the fcc  $\Delta$ DOS. Because of this, the coupling with the UVB states is also changed, the hcp O state coupling more strongly to the CSR2 peak of the substrate UVB, compared to the fcc O state.

In the top site, the adatom–TiSR overlap is larger than in the hcp site, implying a higher value for  $\beta'$ . However, the atomic coordination is lower in the top site. The smaller splitting of the bonding and antibonding adatom–TiSR states can therefore be understood from the smaller value of the second moment of the adatom LDOS,  $\mu^{(2)} = N\beta'$ , where  $N$  is the coordination of the adatom.

The difference between the top and fcc  $\Delta$ DOS's is much more pronounced than that between hcp and fcc, the main positive peak of the top  $\Delta$ DOS lying 2.2 eV higher than in the fcc  $\Delta$ DOS. Again, the interaction with the substrate UVB is considerably changed because of this, the strongest coupling now being to the main UVB peak (CSR4). Correspondingly, the adatom–UVB coupling is more localized around the surface-bilayer Ti atoms than the C atoms. This is also due to the site geometry, which makes overlap with C-localized states negligible. Still, though, some clear O–C coupling is detected in the lower part of the main positive  $\Delta$ DOS peak, showing that the adatom–CSR coupling is weakly active also for top O.

We conclude that the concerted-coupling model is capable of explaining the electronic-structure features for adsorption in hcp and top sites as well. Like for the fcc site, the chemisorption in hcp and top sites can be described as composed of two interacting components: an adatom–TiSR coupling and an adatom–CSR coupling.

(f) *O adatom on TiC(001)*. Since the nonpolar TiC(001) surface lacks the TiSR characteristic of the polar (111) surface [Sec. III.B.3], a comparison between the electronic structures of O adsorbed on the two surfaces can provide some information on the importance of the TiSR for the adsorption.

Our calculated  $\Delta$ DOS for O in the most favorable TiC(001) site (on-top C) shows the presence of only one negative peak (Fig. 24), which lies just above the main peak of the substrate UVB and is mainly localized around the substrate C atom. Thus, only one type of coupling is present here, between the adatom state and C-localized states in the upper part of the substrate UVB. As discussed above [Sec. III.B.3], this is the only UVB region

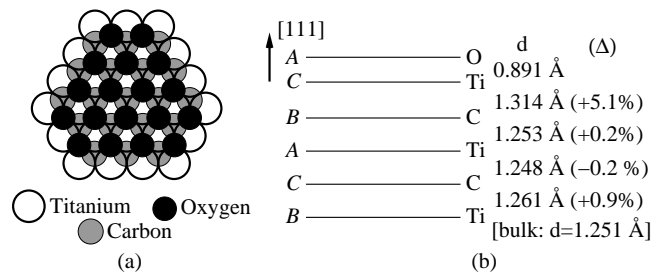


FIG. 26: Structure of TiC(111)-O(1 × 1): (a) top view of the three top surface layers; (b) the top six surface layers, seen perpendicularly to [111], showing the stacking sequence and the interlayer relaxations, in absolute values ( $d$ ) and relative to the TiC bulk distance ( $\Delta$ ), calculated with our 15-bilayer slab (see Sec. II).

that shows signs, in our results, of SR's. The  $\Delta$ DOS shows that this coupling forms bonding peaks just below the UVB region, of mixed O and C character, and an antibonding region around and above  $E_F$ .

Thus, the weaker adsorption on TiC(001), compared to TiC(111), can be understood to arise from a lack of coupling to Ti-centered SR's on (001).

#### D. Oxygen (1 × 1) monolayer on TiC(111)

So far, experimental studies of adsorption on TiC(111) have primarily been concerned with full oxygen (1 × 1) monolayer coverage.<sup>25,28</sup> Therefore, we conclude our investigation with calculations on the O monolayer on TiC(111). As for the case of atomic adsorption, first, the adsorption energetics and geometry are investigated. Then, the electronic structure is analyzed in order to understand the bonding nature. In particular, we consider to what extent our concerted-coupling model for atomic chemisorption can be used in the situation of full monolayer coverage.

##### 1. Energetics and geometry

On TiC(111), full monolayer coverage of O(1 × 1) has been observed experimentally.<sup>25</sup> The unreconstructed O(1 × 1) structure is reported to be stable up to approximately 1000°C, where it starts to reconstruct to  $(\sqrt{3} \times \sqrt{3})$ -R30°. The O(1 × 1) atoms are found to occupy the hollow sites with no C directly underneath, that is, the fcc sites [see Fig. 26(a)].<sup>25</sup>

Our calculated adsorption energies for O(1 × 1) in both hollow sites (fcc and hcp) and in top site (Table V) agree with the experimental results of the fcc site being the stable one.

According to our calculations, the TiC(111) surface relaxation is significantly affected by the fcc O overlayer. The four top interlayer relaxations of TiC(111) (as calculated with our 15-bilayer slab, see Sec. II) are now:

TABLE V: Adsorption energies  $E_{\text{ads}}$  for a full monolayer of O ( $1 \times 1$ ) on TiC(111), as calculated with our 15-bilayer slab (see Sec. II). Adsorption in fcc, hcp, and top sites is considered.

$E_{\text{ads}}$ [eV/atom]		
fcc site	hcp site	top site
8.12	7.31	5.48

+5.1%, +0.2%, -0.2%, and +0.9% [Fig. 26(b)], as compared to the values -19.2%, +11.0%, -5.8%, and +0.6% for the clean TiC(111) surface [Fig. 5(b)]. The distance between the O layer and the TiC(111) surface is 0.891 Å. The O-Ti bond is thus quite strong, pulling up the top Ti layer away from the second C layer and toward the chemisorbed O layer. Also, we note that the relaxation is limited to the first surface layer (the interlayer distances change by less than 0.02 Å from the second TiC bilayer on).

The ICISS study of Souda *et al.*<sup>25</sup> reports about the presence of two different O sites, with different Ti-O interlayer distances (1.0 Å and 0.8 Å, respectively). No sign of this is present in our results, our calculated interlayer distance lying in the middle of these two values. We stress here that the convergence of our calculations has been carefully tested and that full relaxation using both a ( $1 \times 1$ ) and a ( $2 \times 3$ ) surface unit cell has been performed [see Sec. II for details]. In addition, the calculation with the ( $2 \times 3$ ) cell has been performed both with and without symmetry constraints on the calculated KS wavefunctions.

Our relaxed O-Ti and O-C bond lengths are 1.98 Å and 2.83 Å, respectively.

## 2. Electronic Structure

Like for the case of atomic adsorption, we now turn to the analysis of the electronic structure for full ( $1 \times 1$ ) monolayer of O on TiC(111), in order to understand the nature of the bond.

In particular, the calculated  $\Delta$ DOS for fcc O( $1 \times 1$ ) (Fig. 27) is compared with that for the fcc O adatom (Fig. 17). For fcc O( $1 \times 1$ ), we note that (i) the negative peak around  $E_F$  is broadened and consists of a single peak, at +0.1 eV, of almost exclusively Ti  $d_{(xz,yz)}$  and  $d_{(xy,x^2-y^2)}$  character; (ii) the positive peak in the low-energy part of the UVB is broadened and split into two subpeaks, at -5.2 and -4.4 eV, of almost exclusively O character (the smaller peak, at -5.2 eV, has almost exclusively O  $p_{xy}$  symmetry); (iii) smaller positive peaks are present at -3.4 eV (of mainly O  $p_z$  symmetry), at -2.1 eV (of mainly O  $p_z$  and C  $p_z$  symmetry), and at -1.1 eV (of mainly C  $p_z$  symmetry).

The DOS( $\mathbf{r}, E$ ) plots for the fcc O ( $1 \times 1$ ) monolayer show that (i) the peak at -5.2 eV is composed of O-O, O-Ti, and O-C bonding states; (ii) the peak at -4.4 eV is composed of O-Ti and O-C bonding states; (iii)

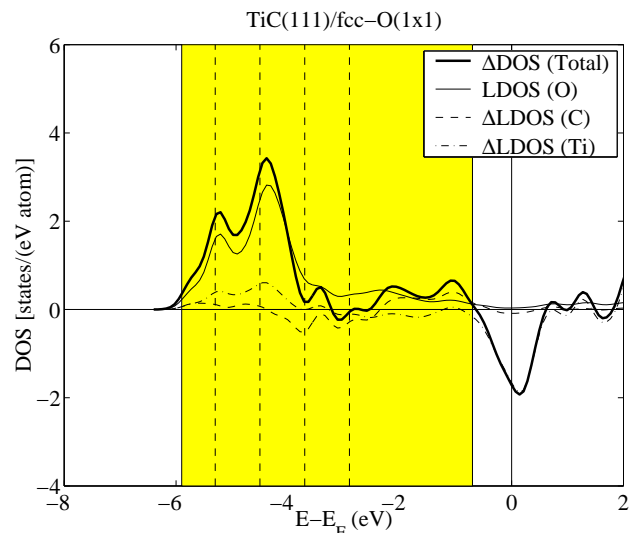


FIG. 27: Same as Fig. 14 but for a full ( $1 \times 1$ ) monolayer of O atoms adsorbed in the fcc sites of the TiC(111) surface.

the remaining positive peaks contain only O-Ti bonding states.

These results agree with experimental studies that show that the O  $p_{xy}$  orbitals lie at lower energy than the O  $p_z$  orbitals.<sup>28</sup>

## 3. Analysis of the Electronic Structure

Our calculated  $\Delta$ DOS (Fig. 27) shows a strong depletion of states in the energetical region of the TiSR. This indicates that the adatom-TiSR coupling is active also in the case of full monolayer ( $1 \times 1$ ) adsorption of O on TiC(111). In addition, the DOS( $\mathbf{r}, E$ ) plots show the presence of adatom-C bonding states in the low-energy region of the UVB, implying that the adatom-CSR coupling is also still present. Thus, our concerted-coupling model appears to be valid also for the case of full monolayer coverage of O on TiC(111).

However, the calculated  $\Delta$ DOS for O( $1 \times 1$ ) adsorption shows a considerably stronger broadening of the adatom  $p$  peak than for atomic O (Fig. 17), as well as a splitting of the adatom  $p$  peak into two subpeaks. The DOS( $\mathbf{r}, E$ ) plots show that O-O bonding states are present in the lower subpeak and absent in the higher subpeak. Thus, the broadening and splitting of the  $p$  peak arise from the coupling between neighboring O atoms within the O monolayer, which gives rise to the formation of bonding and antibonding O-O states. The bonding O-O states dominate in the lower part of the O  $p$  peak, while antibonding O-O states dominate in the upper part of the O  $p$  peak.

It is interesting to notice that the O  $p_{xy}$  states are more important for the most bonding states, while the O  $p_z$  states are more important at higher energies. Obviously, the O  $p_{xy}$  states overlap more strongly with the neighbor-

ing O atoms in the monolayer, thus providing stronger binding. However, the O  $p_{xy}$  states are more bonding also in the case of atomic adsorption (as discussed in Secs. III.C.2 and III.C.3) and are therefore more favorable also for the coupling with the TiC(111) surface. This can be understood by considering that the O adatom lies in the fcc site, that is, in the middle of the two triangles formed by the NN Ti and C atoms. Thus, the interaction with the NN Ti and C atoms is predominantly lateral, as exemplified by Figs. 15(a)–(b), and as discussed also in Sec. III.C.3(c).

#### IV. DISCUSSION

In the previous sections, a concerted-coupling model is presented to describe the mechanisms behind chemisorption on the polar TiC(111) surface. The model is based on detailed analyses, within the theoretical framework of the Newns-Anderson (NA) model, of the electronic structures for the clean surface, for first-, second-, and third-period adatoms in fcc site, for the O adatom in hcp and top sites, and for a full ( $1 \times 1$ ) monolayer coverage of O. Also, for comparison, O adsorption on the nonpolar TiC(001) surface is considered.

According to this model, chemisorption on TiC(111) is caused by the combination of two different types of adatom–substrate couplings: (i) a strong, in the NA sense, coupling between the adatom state(s) and the Ti-localized SR (TiSR) of TiC(111) and (ii) a coupling, whose strength varies significantly between the different adatoms, between the adatom state(s) and the TiC(111) UVB states, in particular the C-localized SR’s (CSR’s) in the low-energy part of the UVB.

At the same time, our calculations yield characteristic, pyramid-like, trends for the atomic fcc adsorption energies  $E_{\text{ads}}$  within each adatom period, with strongest adsorption for the group-VI elements (O and S). In particular, the adsorption energy for fcc O adatom is very high, almost 9 eV/adatom, reflecting the high reactivity of the polar TiC(111) surface.

In this section, we discuss how the concerted-coupling model can provide an understanding of these adsorption-energy trends and of the extremely large variations of adsorption energies between adatoms (from 3.4 eV/adatom for fcc Al to 8.8 eV/adatom for fcc O) and between surface orientations [the  $E_{\text{ads}}$  value for O on TiC(001) being 43% smaller than on TiC(111)].

In particular, we wish to address the following questions: (i) How can we understand the  $E_{\text{ads}}$  trends within each adatom period? (ii) How can we understand the lower  $E_{\text{ads}}$  values for third-period adatoms? (iii) Why is chemisorption strongest in the fcc site? (iv) Why is chemisorption stronger on TiC(111) than on TiC(001)?

In the following, the trends in our calculated electronic structures for the considered systems are qualitatively correlated to the calculated  $E_{\text{ads}}$  trends. In this way, we identify features in the concerted-coupling model that

can be used to understand the calculated  $E_{\text{ads}}$  trends.

In order to answer question (i), we start by examining the second-period adatoms. As discussed in Sec. III.C.3(c), as the adatom nuclear charge  $Z$  increases within the period, the two components of the concerted coupling vary, in different ways.

The variations in area of the negative  $\Delta$ DOS peaks around  $E_F$  indicate variations in the adatom–TiSR coupling strength: slightly increasing as  $B \rightarrow C$  and strongly decreasing as  $C \rightarrow N \rightarrow O \rightarrow F$ . The strong decrease from C to F can be understood as a consequence of the decreasing energetical overlap between the adlevel and TiSR energies, which decreases the strength of the adatom–TiSR coupling. The slight increase from B to C is based on a widening of the negative  $\Delta$ DOS peak due to the downward shift of the main positive peak. Thus, it may simply be due to a cancellation effect between the positive and negative peaks of B, which partially overlap.

Thus, the trend in chemisorption strength that arises from the adatom–TiSR coupling can be qualitatively illustrated as in Fig. 28(a), where we allow an uncertainty in the  $B \rightarrow C$  trend.

On the other hand, the total strength of the adatom–CSR couplings increases as the adlevel energy approaches the energy of the CSR’s, that is, the region between the main substrate-UVB peak (CSR4) and the lower edge of the substrate UVB. The best energetical overlap between the adlevel and the CSR’s is obtained for the O adatom, for which all positive  $\Delta$ DOS peaks of adatom  $p$  symmetry below  $E_F$  lie in the CSR region.

Thus, the trend in chemisorption strength that arises from the adatom–CSR coupling can be qualitatively illustrated as in Fig. 28(b).

As can be seen, the adatom–TiSR trend does not agree with the  $E_{\text{ads}}$  trend, while the adatom–CSR does. We conclude that, in order to reproduce the calculated trend in adsorption energy for the second-period adatoms, a description in which both the adatom–TiSR and adatom–CSR couplings are present is needed. In particular, our analysis points toward the novel result that *the C-localized states in the lower part of the TiC UVB, although less important for the bonding nature in bulk TiC, play an important role in the description of the nature of chemisorption on the TiC(111) surface.*

We also note that the almost constant value of  $E_{\text{ads}}$  between C and N can be explained by the fact that the two coupling-strength trends go in opposite directions as  $C \rightarrow N$ .

For the third-period adatoms, the variations in coupling-strength trends follow similar trends to those described above for the second period [see Sec. III.C.3(d)]. The main difference is due to the higher energy of the third-period free-adatom level, which causes a better overlap with the CSR’s for Cl than for S, in contrast to our calculated  $E_{\text{ads}}$  trend. As discussed in Sec. III.C.3(d), however, a weakening of the Cl–CSR coupling is introduced by the fact that the Cl adatom is almost fully ionized.

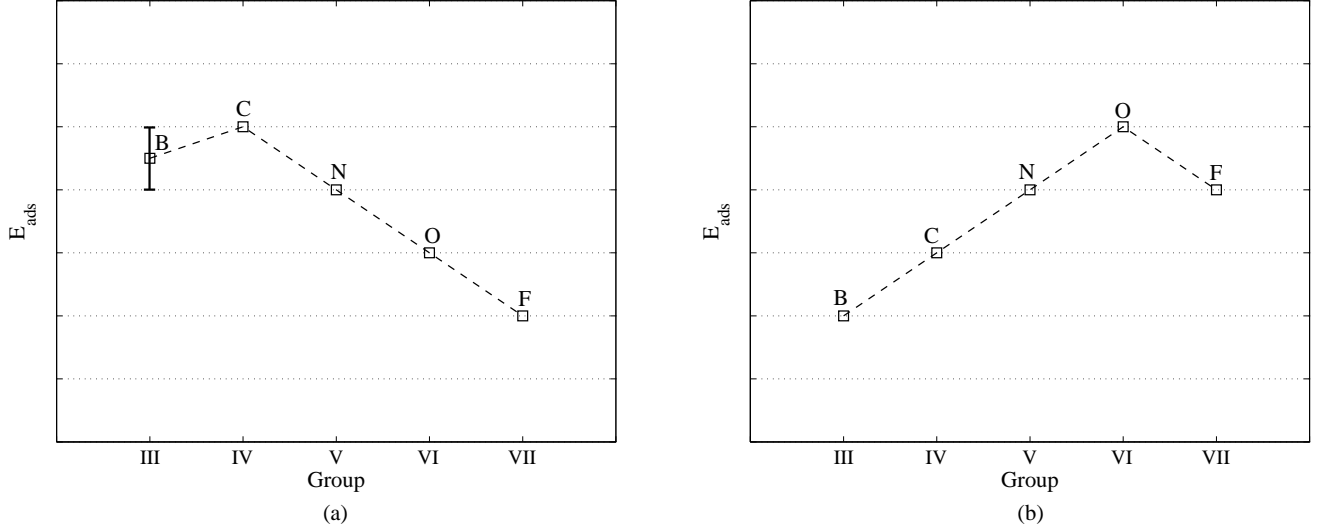


FIG. 28: Qualitative graph of the suggested trends in adsorption energy  $E_{\text{ads}}$  for the second-period adatoms caused by (a) the adatom-TiSR coupling and (b) the adatom-CSR couplings. In (a), the uncertainty in the  $B \rightarrow C$  trend (see text for details) is marked by an error bar.

Finally, we comment on the presence of couplings with the CSR's for the B and Al  $s$  states [described in Secs. III.C.3(c)-(d)]. In the same way as for the coupling between the CSR's and the  $p$  states of Cl, it should be expected that a coupling between CSR's and adatom  $s$  states is weak, due to the filled nature of the  $s$  electron shells for B and Al.

Question (ii) can now be simply understood. As discussed in Sec. III.C.3(d), two main differences, both due to core orthogonalization, can be detected between the electronic structures of the second- and third-period adatoms: overall smaller negative  $\Delta\text{DOS}$  peaks around  $E_F$  for the third-period adatoms and overall higher energies for the positive  $\Delta\text{DOS}$  peaks below  $E_F$  for the third-period adatoms. The first difference indicates a weaker adatom-TiSR coupling for the third-period adatoms. The second difference causes, within an adatom group, a weaker energetical overlap between adlevel and CSR's for the third-period adatoms. Thus, both the coupling to the TiSR and to the CSR's are weaker for period-three adatoms, in agreement with our calculated  $E_{\text{ads}}$  trends.

Question (iii) can also be answered through the concerted-coupling model. As discussed in Sec. III.C.3(e), the preference for fcc site over hcp site is due to the spatial extension of the TiSR, which extends toward the fcc site and avoids the hcp site. The resulting smaller spatial overlap between hcp adatom state and TiSR, compared to the fcc adatom, causes a weaker adatom-TiSR coupling. This in turn causes a smaller downward shift of the bonding adatom-TiSR state and consequently also a weaker coupling between the adatom state and the CSR's. Thus, both the adatom-TiSR and adatom-CSR couplings are weaker in the hcp site than in the fcc site.

For the top adatom, the lower adatom coordination causes a considerably smaller downward shift of the adatom-TiSR bonding state than for both hcp and fcc adatoms, again weakening the chemisorption strength. Also, due to the top-site geometry, the spatial overlap between the top-adatom state and the C-localized states is negligible, thus strongly weakening also the adatom-CSR coupling.

Finally, question (iv) can be simply understood [Sec. III.C.3(f)] from the lack of a TiSR on the TiC(001) surface. Thus, one of the couplings present on the TiC(111) surface is here absent, causing a considerably weaker chemisorption.

In summary, the concerted-coupling model can be used to successfully explain the essential features of the calculated  $E_{\text{ads}}$  trends. In particular, the coupling of the adatom state to the C-localized states (CSR's) of the TiC(111) surface is expected to play an important role for the chemisorption trends on this surface. This is qualitatively different from the case of, *e.g.*, adsorption on transition-metal surfaces, where the weak coupling to the  $sp$  band does not affect the adsorption trends.

## V. CONCLUSIONS

Chemisorption of atoms in the first three periods in the table of elements (H, B, C, N, O, F, Al, Si, P, S, and Cl) on the polar TiC(111) surface, as well as of atomic O on the nonpolar TiC(001) surface and of full ( $1 \times 1$ ) monolayer coverage of O on TiC(111) are studied in a systematic way by density-functional theory. Adsorption energies and geometries are calculated in fully relaxed configurations. Detailed analyses of the electronic struc-

tures of the different systems, as well as of bulk TiC and of the clean TiC(111) and (001) surfaces reveal the nature of chemisorption on this scientifically and technologically interesting material. At the same time, new detailed information is obtained on the electronic structures of bulk and surface TiC, showing, in particular, the presence of direct C–C interactions and of C-localized surface resonances and their importance for the adsorption mechanisms.

The adsorption on TiC(111) is found to be more complex and versatile than on pure metal surfaces. The results for the atomic adsorption energies  $E_{\text{ads}}$  of the second- and third-period elements show strong variations, characterized by pyramid-shaped trends within each period. An extraordinarily high binding energy is obtained for the O atom, 8.8 eV/adatom, followed by C, N, S, and F. The lowest energies are obtained for Al, H, and Si.

To describe the variety in calculated adsorption energies, we propose a concerted-coupling model that involves the concerted action of two different types of couplings: (i) between the adatom state(s) and the Ti-centered Fermi-level surface resonance (TiSR) of TiC(111) and (ii) between the adatom state(s) and the C-centered surface resonances (CSR's) lying in the lower part of the TiC(111) upper valence band (UVB).

This model explains successfully the essential features of the calculated trends in  $E_{\text{ads}}$ . For example, the exceptionally strong chemisorption of O is understood to arise from this combination of two different adsorption mechanisms.

The strong variations in adsorption strengths show the versatility of TiC for technological applications. The strong O adsorption makes TiC(111) a good substrate for oxide-layer growth, a fact that is used in multilayer CVD (chemical-vapor deposition) alumina/Ti(C,N) coatings on wear-resistant cutting tools. At the same time, the high  $E_{\text{ads}}$  value for S suggests it to be a strong candidate in the competition for adsorption sites, which can explain the presence of S found in the CVD alumina coat-

ings under certain conditions, affecting the alumina phase composition.<sup>72</sup>

Although proper bulk and growth calculations obviously are needed, our calculated diffusion-barrier estimates might be indicative for the synthesis and properties of the MAX phases. Their good plasticity relates to a weak bonding between the (111) face of Ti<sub>6</sub>C layers and, *e.g.*, Al or Si.<sup>13</sup> Our diffusion-barrier estimates for Al and Si (of the order of 0.1–0.3 eV, corresponding to activation temperatures of  $\sim 50$ –130 K)<sup>73</sup> suggest good lateral mobility between the Al/Si and Ti<sub>6</sub>C layers.

The fundamental nature of the concerted-coupling model, based on the Newns-Anderson model, should make it apt for general application to transition-metal carbides and nitrides. In separate publications, the adsorption features and electronic structures of TiN(111) are compared to those for TiC(111), showing the applicability of the concerted-coupling model also for adsorption on TiN(111).<sup>74,75</sup> For instance, higher diffusion-barrier estimates are found on TiN(111), which might provide ideas for the fine-tuning of the structural composition of the MAX phases.

Further studies addressing these questions would be highly interesting. There are many questions that still remain to be answered.

## Acknowledgments

The study originates from stimulating discussions with Mats Halvarsson. Valuable discussions with Aleksandra Vojvodic and Øyvind Borck are gratefully acknowledged, as are financial support from the Swedish Foundation for Strategic Research via Materials Consortium # 9 and ATOMICS and from the Swedish Scientific Council, and the allocation of computer time at the UNICC facility (Chalmers) and at SNIC (Swedish National Infrastructure for Computing).

\* Electronic address: ruberto@fy.chalmers.se

<sup>1</sup> S.T. Oyama, editor, *The Chemistry of Transition Metal Carbides and Nitrides* (Blackie Academic and Professional, London 1996).

<sup>2</sup> K. Schwarz, *CRC Crit. Rev. Sol. St. Mater. Sci.* **13**, 211 (1987).

<sup>3</sup> H.G. Prengel, W.R. Pfouts, and A.T. Santhanam, *Surf. Coat. Technol.* **102**, 183 (1998).

<sup>4</sup> G. Radhakrishnan, P.M. Adams, R. Robertson, and R. Cole, *Tribol. Lett.* **8**, 133 (2000).

<sup>5</sup> K. Hojou, H. Otsu, S. Furuno, N. Sasajima, and K. Izui, *J. Nucl. Mater.* **239**, 279 (1996); S. Takamura, K. Hayashi, N. Ohno, and K. Morita, *ibid.* **258–263**, 961 (1998).

<sup>6</sup> M.I. Jones, I.R. McColl, D.M. Grant, K.G. Parker, and T.L. Parker, *J. Biomed. Mater. Res.* **52**, 413 (2000).

<sup>7</sup> H.J. Boving and H.E. Hintermann, *Tribol. Intern.* **23**, 129

(1990).

<sup>8</sup> X. Li and B. Bhushan, *Thin Sol. Films* **398–399**, 313 (2001).

<sup>9</sup> W.D. Fan, K. Jagannadham, and B.C. Goral, *Surf. Coat. Technol.* **81**, 172 (1996); M.S. Raghuvver, S.N. Yoganand, K. Jagannadham, R.L. Lemaster, and J. Bailey, *Wear* **253**, 1194 (2002).

<sup>10</sup> H-S. Chen, J.D. Parsons, *Appl. Phys. Lett.* **65**, 2576 (1994).

<sup>11</sup> J. Günster, M. Baxendale, S. Otani, and R. Souda, *Surf. Sci.* **494**, L781 (2001).

<sup>12</sup> N.I. Ilchenko and Yu.I. Pyatnitsky, in *The Chemistry of Transition Metal Carbides and Nitrides*, edited by S.T. Oyama (Blackie Academic and Professional, London 1996); H.H. Hwu and J.G. Chen, *Chem. Rev.* **105**, 185 (2005).



- <sup>13</sup> N.I. Medvedeva, D.L. Novikov, A.L. Ivanovski, M.V. Kuznetsov, and A.J. Freeman, *Phys. Rev. B* **58**, 16042 (1998); Y. Zhou, Z. Sun, X. Wang, and S. Chen, *J. Phys.: Condens. Matter* **13**, 10001 (2001).
- <sup>14</sup> S.A. Jansen and R. Hoffman, *Surf. Sci.* **197**, 474 (1988).
- <sup>15</sup> M. Tsukada and T. Hoshino, *J. Phys. Soc. Jpn.* **51**, 2562 (1982).
- <sup>16</sup> A. Fujimori, F. Minami, and N. Tsuda, *Surf. Sci.* **121**, 199 (1982).
- <sup>17</sup> M. Aono, C. Oshima, S. Zaima, S. Otani, and Y. Ishizawa, *Jpn. J. Appl. Phys.* **20**, L829 (1981).
- <sup>18</sup> C. Oshima, M. Aono, S. Zaima, Y. Shibata, and S. Kawai, *J. Less-Common Metals* **82**, 69 (1981).
- <sup>19</sup> S. Zaima, Y. Shibata, H. Adachi, C. Oshima, S. Otani, M. Aono, and Y. Ishizawa, *Surf. Sci.* **157**, 380 (1985).
- <sup>20</sup> K.E. Tan, M.W. Finnis, A.P. Horsfield, and A.P. Sutton, *Surf. Sci.* **348**, 49 (1996).
- <sup>21</sup> A.M. Bradshaw, J.F. van der Veen, F.J. Himpsel, and D.E. Eastman, *Sol. St. Comm.* **37**, 37 (1980).
- <sup>22</sup> K. Edamoto, T. Anazawa, A. Mochida, T. Itakura, E. Miyazaki, H. Kato, and S. Otani, *Phys. Rev. B* **46**, 4192 (1992).
- <sup>23</sup> J. Ahn, H. Kawanowa, and R. Souda, *Surf. Sci.* **429**, 338 (1999).
- <sup>24</sup> K. Edamoto, Y. Abe, T. Ikeda, N. Ito, E. Miyazaki, H. Kato, and S. Otani, *Surf. Sci.* **237**, 241 (1990).
- <sup>25</sup> R. Souda, C. Oshima, S. Otani, Y. Ishizawa, and M. Aono, *Surf. Sci.* **199**, 154 (1988).
- <sup>26</sup> C. Oshima, M. Aono, S. Otani, and Y. Ishizawa, *Sol. St. Comm.* **48**, 911 (1983).
- <sup>27</sup> K. Edamoto, E. Miyazaki, T. Anazawa, A. Mochida, and H. Kato, *Surf. Sci.* **269/270**, 389 (1992).
- <sup>28</sup> K. Edamoto, A. Mochida, T. Anazawa, T. Itakura, E. Miyazaki, H. Kato, and S. Otani, *Phys. Rev. B* **46**, 7127 (1992).
- <sup>29</sup> P. Hohenberg and W. Kohn, *Phys. Rev.* **136**, B864 (1964); W. Kohn and L.J. Sham, *ibid.* **140**, A1133 (1965).
- <sup>30</sup> B. Hammer *et al.*, Center for Atomic-Scale Materials Physics (CAMP), Danmarks Tekniske Universitet, Lyngby, Denmark.
- <sup>31</sup> K. Burke, J.P. Perdew, and Y. Wang, in *Electronic Density Functional Theory, Recent Progress and New Directions*, edited by J.F. Dobson, G. Vignale and M.P. Das (Plenum Press, New York and London 1998); pp. 81–111.
- <sup>32</sup> D. Vanderbilt, *Phys. Rev. B*, **41**, 7892 (1990).
- <sup>33</sup> H.J. Monkhorst and J.D. Pack, *Phys. Rev. B* **13**, 5188 (1976).
- <sup>34</sup> L. Bengtsson, *Phys. Rev. B* **59**, 12301 (1999).
- <sup>35</sup> L. Bengtsson, *Efficient Density-Functional-Based Computational Methods for Surfaces*, Ph.D. Thesis (Chalmers University of Technology and Goteborg University, Goteborg, Sweden 1999); pp. 40–3.
- <sup>36</sup> Y. Yourdshahyan, C. Ruberto, M. Halvarsson, L. Bengtsson, V. Langer, B.I. Lundqvist, S. Ruppi, and U. Rolander, *J. Am. Ceram. Soc.* **82**, 1365 (1999).
- <sup>37</sup> C. Ruberto, Y. Yourdshahyan, and B.I. Lundqvist, *Phys. Rev. Lett.* **88**, 226101 (2002); *Phys. Rev. B* **67**, 195412 (2003).
- <sup>38</sup> S. Dudiy, J. Hartford, and B.I. Lundqvist, *Phys. Rev. Lett.* **85**, 1898 (2000).
- <sup>39</sup> H. Rydberg, M. Dion, N. Jacobson, E. Schröder, P. Hyldgaard, S.I. Simak, D.C. Langreth, and B.I. Lundqvist, *Phys. Rev. Lett.* **91**, 126402 (2003).
- <sup>40</sup> R.F.W. Bader, *Chem. Rev.* **91**, 893 (1991).
- <sup>41</sup> N.O.J. Malcolm and P.L.A. Popelier, *J. Comput. Chem.* **24**, 1276 (2003).
- <sup>42</sup> J.G. Gay, J.R. Smith, R. Richter, F.J. Arlinghaus, and R.H. Wagoner, *J. Vac. Sci. Technol. A* **2**, 931 (1984).
- <sup>43</sup> J.C. Boettger, *Phys. Rev. B* **49**, 16 798 (1994).
- <sup>44</sup> V. Fiorentini and M. Methfessel, *J. Phys.: Condens. Matter* **8**, 6525 (1996).
- <sup>45</sup> J.C. Boettger, *Phys. Rev. B* **53**, 13 133 (1996).
- <sup>46</sup> C. Ruberto, *Metastable Alumina from Theory: Bulk, Surface, and Growth of  $\kappa$ -Al<sub>2</sub>O<sub>3</sub>*, Ph.D. Thesis (Chalmers University of Technology and Göteborg University, Göteborg, Sweden 2001).
- <sup>47</sup> A. Dunand, H.D. Flack, and K. Yvon, *Phys. Rev. B* **31**, 2299 (1985).
- <sup>48</sup> H. Ihara, Y. Kumashiro, and A. Itoh, *Phys. Rev. B* **12**, 5465 (1975).
- <sup>49</sup> L.I. Johansson, P.M. Stefan, M.L. Shek, and A.N. Christensen, *Phys. Rev. B* **22**, 1032 (1980).
- <sup>50</sup> P. Blaha and K. Schwarz, *Int. J. Quant. Chem.* **23**, 1535 (1983).
- <sup>51</sup> P. Blaha, J. Redinger, and K. Schwarz, *Phys. Rev. B* **31**, 2316 (1985).
- <sup>52</sup> D.L. Price and B.R. Cooper, *Phys. Rev. B* **39**, 4945 (1989).
- <sup>53</sup> M.E. Eberhart and J.M. MacLaren, in *The Chemistry of Transition Metal Carbides and Nitrides*, edited by S.T. Oyama (Blackie Academic and Professional, London 1996), Chap. 5.
- <sup>54</sup> S.-H. Jhi, J. Ihm, S.G. Louie, and M.L. Cohen, *Nature* **399**, 132 (1999).
- <sup>55</sup> S.F. Matar, Y. Le Petitcorps, and J. Etourneau, *J. Mater. Chem.* **7**, 99 (1997).
- <sup>56</sup> P.W. Tasker, *J. Phys. C* **12**, 4977 (1979).
- <sup>57</sup> D.L. Price, J.M. Wills, and B.R. Cooper, *Phys. Rev. Lett.* **77**, 3375 (1996).
- <sup>58</sup> M. Tagawa, T. Kawasaki, C. Oshima, S. Otani, K. Edamoto, and A. Nagashima, *Surf. Sci.* **517**, 59 (2002).
- <sup>59</sup> G. Kresse and J. Furthmüller, *Phys. Rev. B* **54**, 11 169 (1996); *Comput. Mater. Sci.* **6**, 15 (1996); G. Kresse and J. Hafner, *Phys. Rev. B* **49**, 14 251 (1994); **48**, 13 115 (1993); **47**, 558 (1993).
- <sup>60</sup> S.V. Dudiy and B.I. Lundqvist, *Phys. Rev. B* **69**, 125421 (2004).
- <sup>61</sup> C. Oshima, M. Aono, T. Tanaka, S. Kawai, S. Zaima, and Y. Shibata, *Surf. Sci.* **102**, 312 (1981).
- <sup>62</sup> R. Souda, T. Aizawa, S. Otani, Y. Ishizawa, and C. Oshima, *Surf. Sci.* **256**, 19 (1991).
- <sup>63</sup> S.V. Didzilius, K.D. Butcher, and S.S. Perry, *Inorg. Chem.* **42**, 7766 (2003).
- <sup>64</sup> Y.-F. Zhang, J.-Q. Li, and Z.-F. Liu, *J. Phys. Chem. B* **108**, 17143 (2004).
- <sup>65</sup> See, *e.g.*, B.I. Lundqvist, in *Interaction of Atoms and Molecules with Solid Surfaces*, edited by V. Bortolani, N.H. March, and M.P. Tosi (Plenum Press, New York and London, 1990), Chap. 8.
- <sup>66</sup> D.M. Newsn, *Phys. Rev.* **178**, 1123 (1969).
- <sup>67</sup> P.W. Anderson, *Phys. Rev.* **124**, 41 (1961).
- <sup>68</sup> D. Spanjaard and M.C. Desjonquères, in *Interaction of Atoms and Molecules with Solid Surfaces*, edited by V. Bortolani, N.H. March, and M.P. Tosi (Plenum Press, New York and London 1990), Chap. 9.
- <sup>69</sup> B. Hammer and J.K. Nørskov, *Surf. Sci.* **343**, 211 (1995); **359**, 306 (1996).
- <sup>70</sup> K. Stokbro and S. Baroni, *Surf. Sci.* **370**, 166 (1997).
- <sup>71</sup> B. Hammer and J.K. Nørskov, in *Advances in Catalysis*,

edited by B.C. Gates and H. Knözinger (Academic Press, San Diego and London 2000), Vol. 45, p. 71.

<sup>72</sup> M. Halvarsson, A. Larsson, and S. Rупpi, *Micron* **32**, 807 (2001).

<sup>73</sup> A. Bogicevic, J. Strömquist, and B.I. Lundqvist, *Phys. Rev. Lett.* **81**, 637 (1998).

<sup>74</sup> A. Vojvodic, C. Ruberto, and B.I. Lundqvist, submitted to *Surf. Sci.* (2005).

<sup>75</sup> C. Ruberto, A. Vojvodic, and B.I. Lundqvist, submitted to *Surf. Sci.* (2005).

<sup>76</sup> Note that this TiSR has been called surface state in the literature, but we prefer here to adopt the proper term surface resonance (SR), since its energy lies in the pseudo-gap between the bulk UVB and CB, that is, in a region of nonzero bulk DOS.